Sigma Coordinate Pressure Gradient Errors and the Basin Problem

Master Thesis in Applied Mathematics

Borghild Ness

Department of Mathematics
University of Bergen

April 15, 2010

I would like to thank my supervisor Jarle Berntsen for all help and advice.

Borghild Ness,
Bergen, April 2010

Contents

Introduction

In ocean modelling there are several categories of numerical models. By investigating the vertical coordinates in the models, one find that most of them can be classified as either Cartesian (z), isopycnal (ρ) or terrain following (σ) models, see Figures 1, 2 and 3, respectively. The models are analogous in their continuous form, but the discretisations make the systems different [Haidvogel and Beckmann, 1999]. Similar problems may therefore get different answers. Since large errors in simulations often can be traced back to the choice of vertical coordinates, the pros and cons of the different coordinates are of great importance.

3D ocean models

The first ocean models used z-coordinates in the vertical, see Figure 1. Equations then assume their familiar form. In these coordinates, the surface and bottom layer processes are difficult to resolve. The reasons are, respectively, the thickness of the surface layer (that has to be chosen larger than the largest amplitude of the free surface), and the stepwise representation of the bottom topography. In addition, an artificial diapycnal diffusion leads to a false stratification along z-surfaces [Haidvogel and Beckmann, 1999]. A favourable aspect is that the hydrostatic balance is easy to compute. This is important for the long term thermohaline circulation.

In density layer models (Figure 2), the artificial diapycnal diffusion is almost zero. The reason is that most of the transports in the oceans occur approximately along isopycnal surfaces. In contradiction to the z- and σ-coordinates, these coordinates maintain the internal fronts between water masses in long-time integrations. The difference lies in the time-dependent grid that can, in principle, adjust to the dynamic situation of the ocean [Haidvogel and Beckmann, 1999]. Following the pros above are two less favourable aspects; The resolution near bottom and surface, and the estimations of the internal pressure.

Terrain-following (σ-coordinate) models are widely used, see Figure 3.

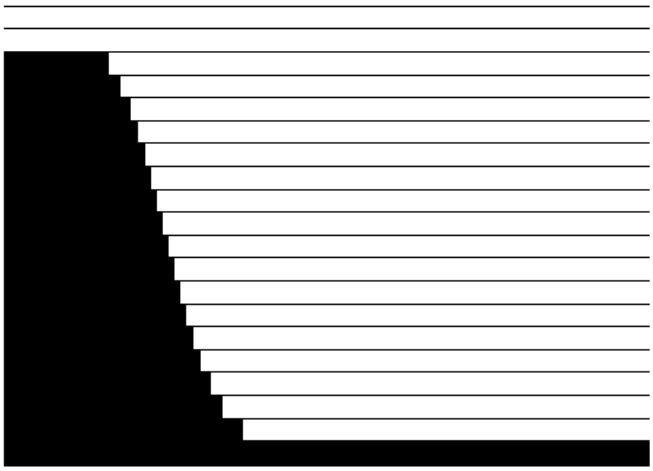

Figure 1: Vertical discretisation for an equidistant z-coordinate model in 2D; Lines constant z; Black bottom topography.

They are often advantageous when dealing with large variations in topography [Mellor et al., 1998], and give an accurate representation of the bottom and top boundary layers. However, near steep topography the use of these coordinates can lead to large errors in the pressure gradient force. The horizontal pressure gradient in the σ-coordinate system consists of two terms, which may be large, comparable in magnitude, and opposite in sign. A small error in one of these terms can ultimately lead to an unacceptable result. If the internal pressure gradient errors are understood and hopefully reduced, the σ-coordinates may give superior ocean models.

Prior work

The severity of the pressure gradient errors in σ-coordinates is a topic of discussion. According to Haney [1991], the scheme is hydrostatically consistent if

$$\left| \frac{\sigma}{\delta\sigma} \frac{\delta D}{D} \right| < 1 \,. \tag{1}$$

Here, σ is the vertical sigma coordinate (see Chapter 1), $\delta\sigma$ is the vertical grid size, δD is the horizontal change of depth between two neighbouring cells

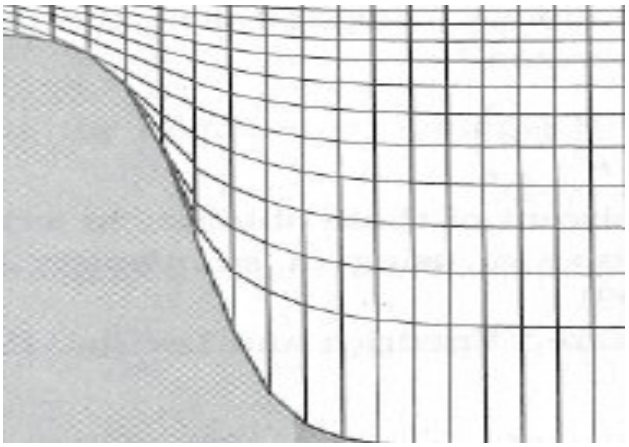

Figure 2: Vertical discretisation for an isopycnal coordinate model in 2D [Haidvogel and Beckmann, 1999]

and $D = h + \eta$ where h is the static depth and η is the free surface elevation. By letting $\delta\sigma$ tend to zero, one would expect to improve the results, but this is impossible without violating Equation (1) closer to the bottom boundary.

Mellor et al. [1994] pointed out that criterion in Equation (1) is very restrictive. They showed that the discretisation error for the second-order internal pressure method used in POM is to leading order

$$E\left(\frac{\delta_x b}{\delta x}\right) = \frac{D}{4}\frac{\delta_x D}{\delta x}\left(\frac{\partial^2 b}{\partial z^2}\right)\left[(\delta\sigma)^2 - \sigma^2\left(\frac{\delta_x D}{D}\right)^2\right] , \tag{2}$$

where x is the horizontal coordinate, z the vertical coordinate and $b = \frac{\rho g}{\rho_0}$ is the buoyancy. Here g is the gravity constant, ρ is the density and ρ_0 is a constant reference density. In contrast to Equation (1), Equation (2) shows that the error decreases if $\delta\sigma$ and $\frac{\delta_x D}{D}$ goes to zero. Hydrostatic consistency is accordingly not a useful concept. Increasing the vertical resolution will not help to improve the error if the term involving $\frac{\delta_x D}{D}$ is the limiting factor. After several experiments, Mellor et al. [1994] found that the error is not numerically divergent, and consequently concluded that the pressure gradient error is not of great concern.

There are many different approaches on how to reduce the error in the pressure gradient force. For instance, it is common to subtract the back-

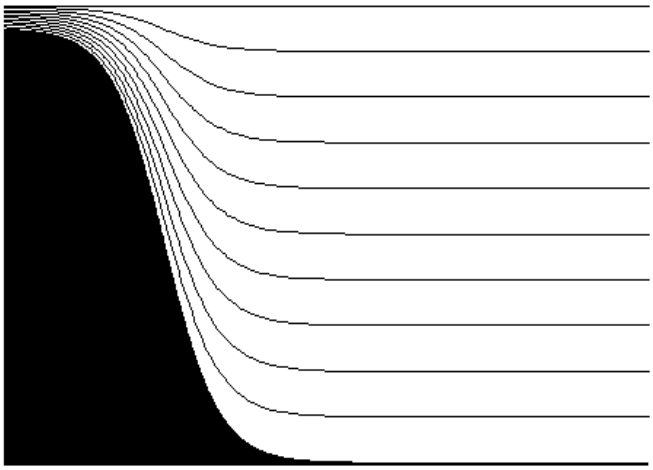

Figure 3: Vertical discretisation for an equidistant terrain-following model in 2D; Lines constant σ; Black bottom topography.

ground stratification that depends only on the vertical coordinate from the density field [Gary, 1973]. One can argue that this will make the remaining terms in the equation smaller and therefore lead to a reduced truncation error. In addition, terms that cancel analytically, but not numerically, can be removed [Haney, 1991; McCalpin, 1994]. However, one can claim that since the "correct" way of splitting the density field is unknown, the validity of these manipulations is uncertain [Shchepetkin and McWilliams, 2003].

Another approach is to compute the internal pressure in z-coordinates, make two estimates of the horizontal pressure gradient, and set it to zero when the results are of opposite sign. If the estimates are of the same sign, the smaller term is used [Stelling and Van Kester, 1994]. While this gives accurate results for the horizontal pycnoline seamount case, it will generally underestimate the true geostrophic flow [Slørdal, 1997].

To reduce the effects of the pressure gradient errors, it is also possible to smooth the topography of the area of study [Barnier et al., 1998]. However, one should keep in mind that altering the topography too much, would mean solving the equations for a different case than the one of interest.

Adding viscosity will dampen the artificial flow caused by the pressure gradient errors. Even though the aberration is limited in the case treated by Mellor et al. [1998], several later studies have suggested that the error

term may grow strongly in cases where more realistic viscosities are applied [Berntsen, 2002]. Generally, it should be a goal to develop ocean models that enable us to study situations as realistic as possible.

Much effort has been put into improving the numerical method used to compute the internal pressure. When McCalpin addressed the seamount case in 1994, he used a fourth order method. Chu and Fan [1997] showed that the error can be further reduced by applying a sixth order method. However, Chu and Fan concluded that there will be little advantage to using the sixth order scheme if the bottom topography is not complex.

Song [1998] advocated the use of a Jacobian representation of the pressure gradient term. He underlined the necessity of the formulation to retain the most important properties of the integral in the continuous case. He, among others, has pointed out that applying the gradient before the integration may reduce the truncation error.

To investigate the internal pressure gradient problem, one can study geostrophic flow [Haney, 1991]. By choosing an appropriate function for ρ, it is possible to find an analytical solution. The error can therefore be found.

Another common experiment is to run a test case of a tall, narrow seamount (first introduced by Beckmann and Haidvogel [1993]). If the isopycnals initially are horizontal, one know that the pressure gradient force and all velocities should be equal zero. Then, if artificial velocities do occur, they will be a measure of the errors. In their work with the seamount, Beckmann and Haidvogel [1993] experienced growing errors for some cases.

When Mellor et al. [1998] studied the seamount case, they classified the errors from the 1994 paper as sigma errors of the first kind (SEFK). SEFK are related to 2D problems, and according to Mellor et al. [1998], they will eventually die out. The growing errors in Beckmann and Haidvogel [1993] were classified as sigma errors of the second kind (SESK). Mellor et al. [1998] relate these to vorticity (relevant to 3D cases), but the SESK observed in their seamount study, decay to a nonzero value.

The thesis

The numerical experiments addressing the seamount case have led to new insight in the nature of the internal pressure gradient errors. In addition, the seamount exercises have led to the development of new and better numerical methods. There are many real seamounts in the ocean. One may therefore argue that the seamount case is a very relevant test case. However, the large scale oceanic flow is strongly connected to the bathymetry of the ocean. It may be reasonable to ask if the lessons learned from the seamount test

enlighten all the errors caused by the internal pressure gradient. Another germane test case may, with a new physical context, reveal errors not previous prominent.

Berntsen et al. [2007] used a test case of the Nordic Seas to investigate the pressure gradient problem. The initial conditions were chosen such that a true solution was known. The results shed light on the order of magnitude of the errors involved, but not on the true errors. The largest errors were observed near the continental shelves.

An alternative way of discretising the Jacobian was introduced by Shchepetkin and McWilliams [2003]. By using Green's theorem, one can evaluate a contour integral instead of a one-dimensional vertical integral. A realistic test case of the Atlantic Ocean was used to compare the new discretisation with the prior approaches to the equation. Their results show that all methods produce the largest errors near the continental shelves.

A common test is to compare the performance of the model to observations. In an attempt to simulate the diurnal stratification cycle in a shallow lake, Condie [1999] experienced that the vertical diffusivity field was characterised by strong peaks over the deep troughs when σ-coordinates were used. The abnormal diffusion was due to errors caused by the internal pressure gradient.

In the realistic test cases above, errors are shown in areas with steep bathymetry. The bottom topography is complex and it is therefore difficult to investigate the reason for the true errors. In this thesis, test cases of idealised 3D ocean basins will be examined. The simplified contexts can be compared to the shape of an ocean or a lake.

This work will focus on how the internal pressure gradient errors affect the numerical instability in idealised ocean basins. The nature of the errors will be investigated and discussed. First, in Chapter 1, the ocean model and the underlying equations will be discussed. In Chapter 2, different forms of ocean basins will be studied. Experiments will show how the shapes affect the generation of false geostrophic flow in the basins. The results here will show the better basin to proceed with in the later experiments. Further on, in Chapter 3, the basin's ability to represent real physical phenomena will be tested. External and internal Kelvin waves will be used as a measure of how well the model works. The SESK will be found in Chapter 4, together with new errors. In Chapter 5 the model's sensitivity to the advection scheme will be tested. An overview of the results and ideas for future investigations are given in Chapter 6.

Chapter 1

Underlying equations and approximations

In the research, the well-known σ-coordinate Princeton Ocean Model (POM) [Blumberg and Mellor, 1987] will be used. The first version of the model was created in the late 1970's by Alan F. Blumberg and George L. Mellor. Today it has more than 3000 users from over 70 different countries.

Any numerical ocean model must be based in some manner on the laws of fluid flow. These can, of course, be simplified, discretised and parametrised etc. in many different ways. In the given chapter some of the principles that POM is built on will be shown. Especially will the pressure term be examined.

1.1 Basic laws for fluid flow

Mass and momentum should always be conserved. Conservation of mass can be expressed as

$$\frac{\partial \rho}{\partial t} + \nabla \cdot (\rho \mathbf{V}) = 0 \ ,$$

where $\mathbf{V}$ is the velocity field $[u, v, w]$, ρ is the density and t is time. This is called the equation of continuity. As for momentum, Newton's second law for fluids can be stated as follows

$$\frac{D\mathbf{V}}{Dt} = -\frac{1}{\rho}\nabla p - 2\mathbf{\Omega} \times \mathbf{V} + \mathbf{g} + \mathbf{F} \ , \tag{1.1}$$

where $\frac{D}{Dt}$ is the total derivative operator, p is the pressure, $\mathbf{\Omega}$ is the earth rotation vector, $\mathbf{g}$ is the gravity, and $\mathbf{F}$ represents other forces. The earth rotation vector $\mathbf{\Omega}$ can be expressed as

$$\mathbf{\Omega} = \Omega \cos(\varphi)\,\mathbf{j} + \Omega \sin(\varphi)\,\mathbf{k} \ ,$$

where Ω is the angular velocity and φ is the latitude. This is the equation of motion (Equation (1.1)) [Gill, 1982].

In component form the equations become

$$\begin{aligned}
x: \qquad \rho\left(\frac{Du}{Dt} + f_* w - f v\right) &= -\frac{\partial p}{\partial x} + \frac{\partial \tau^{xx}}{\partial x} + \frac{\partial \tau^{xy}}{\partial y} + \frac{\partial \tau^{xz}}{\partial z} \ , \\
y: \qquad \rho\left(\frac{Dv}{Dt} + f u\right) &= -\frac{\partial p}{\partial y} + \frac{\partial \tau^{xy}}{\partial x} + \frac{\partial \tau^{yy}}{\partial y} + \frac{\partial \tau^{yz}}{\partial z} \ , \\
z: \qquad \rho\left(\frac{Dw}{Dt} + f_* u\right) &= -\frac{\partial p}{\partial z} - \rho g + \frac{\partial \tau^{xz}}{\partial x} - \frac{\partial \tau^{yz}}{\partial y} + \frac{\partial \tau^{zz}}{\partial z} \ ,
\end{aligned}$$

where

$$f = 2\Omega \sin(\varphi)$$

is the Coriolis parameter,

$$f_* = 2\Omega \cos(\varphi)$$

is the reciprocal Coriolis parameter and τ is the stress tensor. The reciprocal Coriolis parameter is generally very small, and can be set to zero. Here only cases where the variation of the Coriolis force with latitude is negligible are considered, so f will be taken as a constant. In other words, it is assumed that the region is on a f-plane [Cushman-Roisin, 1994].

Here a Cartesian coordinate system, where the positive x, y and z-axis point to the east, north and upwards, respectively is used. The reference level is at $z = 0$, where the water is at equilibrium, $z = -h(x, y)$ is the bottom topography, and the free surface is located at $z = \eta(x, y, t)$.

1.2 Approximations

Following Blumberg and Mellor [1987], two approximations are used to simplify the equations. The first assumption made, is that the density can be split into a mean value ρ_0 and a small perturbation. As a result all density differences that are not multiplied by gravity can be neglected (the Boussinesq approximation). The next approximation is that the pressure at a given depth equals the weight of the water above (the hydrostatic approximation). The equation of continuity becomes

$$\nabla \cdot \mathbf{V} = 0 \ , \tag{1.2}$$

which is equivalent to assuming that the fluid is incompressible [Gill, 1982].

Often it is sufficient to study the statistically averaged flow, leaving aside all turbulence fluctuations. Reynold suggested to divide each variable into a mean and a fluctuation, such as $\mathbf{V} = \overline{\mathbf{V}} + \mathbf{V}_f$ [Pond and Pickard, 1983]. The mean part is found by averaging the value over a time period. Since only mean values are used from now on, bars are dropped. The Reynolds averaged momentum equations [Blumberg and Mellor, 1987] become

$$\begin{aligned}
\frac{\partial u}{\partial t} + \mathbf{V} \cdot \nabla u - fv &= -\frac{1}{\rho_0}\frac{\partial p}{\partial x} + F_x \ , \\
\frac{\partial v}{\partial t} + \mathbf{V} \cdot \nabla v + fu &= -\frac{1}{\rho_0}\frac{\partial p}{\partial y} + F_y \ , \\
\rho g &= -\frac{\partial p}{\partial z} \ .
\end{aligned}$$

Here F_x and F_y represents the small-scale unresolved processes in the x- and y-direction, respectively. They are given by

$$F_x = \frac{\partial}{\partial x}\left[2A_M\frac{\partial u}{\partial x}\right] + \frac{\partial}{\partial y}\left[A_M\left(\frac{\partial u}{\partial y} + \frac{\partial v}{\partial x}\right)\right]$$

and

$$F_y = \frac{\partial}{\partial y}\left[2A_M\frac{\partial v}{\partial y}\right] + \frac{\partial}{\partial x}\left[A_M\left(\frac{\partial u}{\partial y} + \frac{\partial v}{\partial x}\right)\right] \ .$$

A_M is the horizontal viscosity. The diffusivity and the vertical viscosity are set to zero.

In addition to the equations above, an energy equation is needed

$$\frac{D\rho}{Dt} = 0 \ .$$

1.3 The linearised equations

In this study, the linearised version of the stated governing equations will be used [Mellor et al., 1998]. The equation of continuity (Equation (1.2)) is unchanged, while the rest of the governing equations are

$$\frac{\partial u}{\partial t} - fv = -\frac{1}{\rho_0}\frac{\partial p}{\partial x} + F_x \ , \tag{1.3}$$

$$\frac{\partial v}{\partial t} + fu = -\frac{1}{\rho_0}\frac{\partial p}{\partial y} + F_y \ , \tag{1.4}$$

$$\rho g = -\frac{\partial p}{\partial z} \ , \tag{1.5}$$

$$\frac{\partial \rho'}{\partial t} + w\frac{d\rho_{ref}}{dz} = 0 \ . \tag{1.6}$$

Note that the equations have been simplified by splitting the density field ρ

$$\rho(x, y, z, t) = \rho_{ref}(z) + \rho'(x, y, z, t) \ .$$

Here ρ_{ref} is the reference stratification and ρ' is the perturbation density.

By integrating (1.5) from z to the free surface η, the pressure at depth z can be found. The total pressure may be described as

$$p(x, y, z, t) = p_{atm} + p_\eta(x, y, t) + p_{int}(x, y, z, t) \ .$$

Here p_{atm} is the constant atmospheric pressure, $p_\eta = g\rho_0\eta$ is the pressure from the surface elevation and $p_{int} = g\int_z^0 \rho(x, y, z', t)dz'$ is the internal pressure.

To reduce the local errors, the reference stratification ρ_{ref} is subtracted from the density ρ when calculating the internal pressure. The internal pressure used in the POM calculation is therefore

$$p_{int} = g\int_z^0 \rho'(x, y, z', t)dz' \ .$$

Mode splitting

An ocean model should be able to reproduce different physical phenomena. To reduce the computational cost, of resolving fast moving external gravity waves together with for example slow moving internal gravity waves, the model is split in two different modes [Mellor, 2003]. In POM the external mode calculates the vertically integrated equations with small time steps, while the internal mode calculates the full equations with longer time steps [Blumberg and Mellor, 1987].

1.4 Transformation to σ-coordinates

The σ-coordinate models are terrain-following, which means that the vertical layers are shaped after the topography, see Figure 3. Therefore, a transformation from the Cartesian (x, y, z, t) to the σ-coordinates (x^*, y^*, σ, t^*) is needed

$$x^* = x \qquad y^* = y \qquad \sigma = \frac{z-\eta}{h+\eta} \qquad t^* = t \ .$$

Note that $\sigma = 0$ at $z = \eta$ and $\sigma = -1$ at $z = -h$. Let $D \equiv h + \eta$ and apply the chain rule to obtain

$$\begin{aligned}
\frac{\partial G}{\partial x} &= \frac{\partial G}{\partial x^*} - \frac{\partial G}{\partial \sigma}\left(\frac{\sigma}{D}\frac{\partial D}{\partial x^*} + \frac{1}{D}\frac{\partial \eta}{\partial x^*}\right), \\
\frac{\partial G}{\partial y} &= \frac{\partial G}{\partial y^*} - \frac{\partial G}{\partial \sigma}\left(\frac{\sigma}{D}\frac{\partial D}{\partial y^*} + \frac{1}{D}\frac{\partial \eta}{\partial y^*}\right), \\
\frac{\partial G}{\partial z} &= \frac{1}{D}\frac{\partial G}{\partial \sigma} \ , \\
\frac{\partial G}{\partial t} &= \frac{\partial G}{\partial t^*} - \frac{\partial G}{\partial \sigma}\left(\frac{\sigma}{D}\frac{\partial D}{\partial t^*} + \frac{1}{D}\frac{\partial \eta}{\partial t^*}\right),
\end{aligned}$$

where G is an arbitrary field variable.

The following expression for the partial derivative of the pressure that appears in Equation (1.3) is obtained, by using the transformation formulas above

$$\frac{\partial p}{\partial x} = g\int_z^\eta \frac{\partial \rho}{\partial x} dz = gD\int_\sigma^0 \frac{\partial \rho}{\partial x^*} - \frac{\partial \rho}{\partial \sigma}\left(\frac{\sigma}{D}\frac{\partial D}{\partial x^*} + \frac{1}{D}\frac{\partial \eta}{\partial x^*}\right) d\sigma \ .$$

A similar expression is found for the pressure term in Equation (1.4). In this thesis one will focus on the internal pressure gradient

$$\frac{\partial p_{int}}{\partial x} = gD\int_\sigma^0 \left(\frac{\partial \rho'}{\partial x^*} - \frac{\sigma}{D}\frac{\partial \rho'}{\partial \sigma}\frac{\partial D}{\partial x^*}\right) d\sigma \ .$$

Note that ρ_{ref} has been subtracted to reduce errors.

Chapter 2

The test basins

The seamount test case [Beckmann and Haidvogel, 1993] is normally used when studying the numerical instability of the POM code. By applying the model to a new physical context, the errors may force other types of oceanic motion. Two new test cases of idealised ocean basins are chosen, because their shape can be compared to the bathymetry of a real ocean.

2.1 Model setup

Initially, the ocean is at rest with fixed background stratification. There is no physical forcing and the vertical and horizontal diffusivities are zero. In the POM code, the mean density $\rho_0 = 1000\,\mathrm{kg\,m^{-3}}$. The reference exponential stratification ρ_{ref} is given by

$$\rho_{ref}(z) = 28\,\mathrm{kg\,m^{-3}} - \Delta\rho e^{z/500\,\mathrm{m}} \ ,$$

where $\Delta\rho = 3.671\,\mathrm{kg\,m^{-3}}$. Initially the perturbation density ρ' may be defined as

$$\rho'(z) = -1.5\,\mathrm{kg\,m^{-3}} e^{z/500\,\mathrm{m}} \ .$$

Under these circumstances an exact solution is know; zero velocities and no change in density. A way of investigating the errors can therefore be to study the change in the perturbation density ρ'. Another measure for the error is the maximum velocity of the purely artificial flow. The maximum velocity is computed according to

$$V_{max} = \max\left[\sqrt{u_{i,j,k}^2 + v_{i,j,k}^2}\ \right] \ ,$$

where i, j and k are the cell indices in the x-, y- and z-direction, respectively. If a solution is stable, the magnitude of the maximum velocity reach an upper limit.

On the other hand, if the solution is unstable, a Shapiro filter [Shapiro, 1975] can be used to smooth the topography. Then the depth h, at a given grid point in the interior, is replaced by

$$h = 0.25h_L + 0.5h + 0.25h_R \ , \tag{2.1}$$

where h_L and h_R are the depths in the cells to the left and right of the point in the x-direction. The same is done in the y-direction with the new depth h found in Equation (2.1). A less steep slope may give smaller internal pressure gradient errors.

In the seamount test case the slope parameter r is often referred to. This number is a numerical resolution parameter defined by

$$r = \frac{|\partial h|}{2\overline{h}} \ ,$$

where ∂h is the difference in adjacent cell depths and $\overline{h}$ the mean of adjacent depths [Mellor et al., 1998]. If r is not between 0 and 1 the topography is too steep. To avoid instability one then may have to filter or change the bathymetry.

The numerical results depend on the Burger number

$$S = \frac{Nh_0}{fB} \ ,$$

where $h_0 = 4000\,\mathrm{m}$, $B = 40\,\mathrm{km}$, $f = 10^{-4}\,\mathrm{s}^{-1}$ is the Coriolis parameter, g is the gravity and the buoyancy frequency N is given by

$$N^2 = -\frac{g}{\rho_0}\frac{d\rho_{ref}}{dz} \ . \tag{2.2}$$

The uniform grid consist of 120x120 grid cells in the horizontal, where $\Delta x = \Delta y = 20\,\mathrm{km}$. The basin is closed at $x = 0\,\mathrm{km}$, $x = 2400\,\mathrm{km}$, $y = 0\,\mathrm{km}$ and $y = 2400\,\mathrm{km}$.

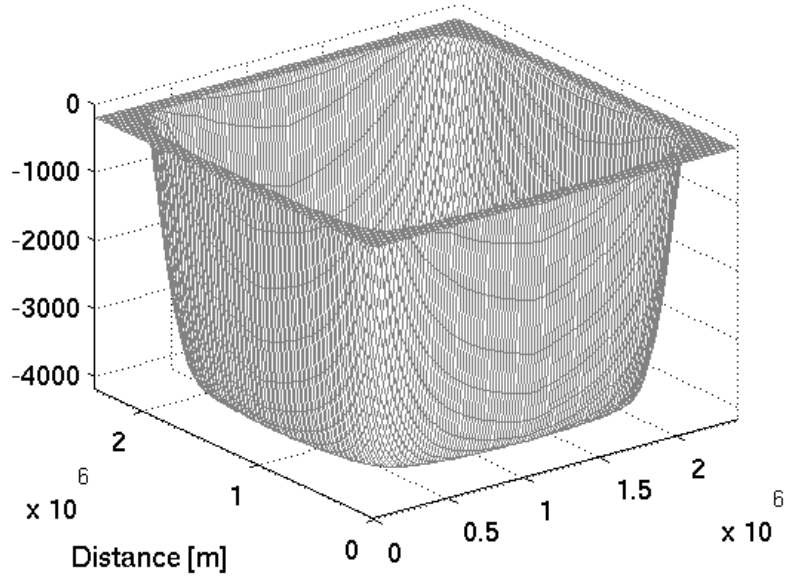

Figure 2.1: The geometry of test basin 1

2.1.1 Basin 1

Bathymetry

The first basin, henceforth referred to as B1, is defined by

$$\begin{aligned} h &= h_s && \text{if } 0 < d < L, \\ h &= h_0 - (h_0 - h_s)\left(\frac{L+s-d}{s}\right)^2 && \text{if } L \leq d \leq L+s\ , \\ h &= h_0 && \text{if } L+s < d, \end{aligned}$$

where L is the width of the shelf, s is the width of the shelf slope, h_s is the depth of the shelf and h_0 is the depth of the deep ocean. In the interior, d is defined by

$$d^{-1} = L_x^{-1} + L_y^{-1}\ .$$

Here L_x and L_y are the distances to the nearest vertical and horizontal boundary at a given point, respectively. At the edges parallel to the x-axis $d = L_y$ and at the edges parallel to the y-axis $d = L_x$. Similar expressions, for finding a number to represent the distance to the closest boundary, are often used in the equations for turbulent closure [Blumberg and Mellor, 1987]. The idealised slope [Gjevik, 2002] has a singularity where the shelf edge meets the parabolic inclination. In this study $L = 100\,\text{km}$, $s = 100\,\text{km}$, $h_s = 200\,\text{m}$ and $h_0 = 4000\,\text{m}$, see Figure 2.1.

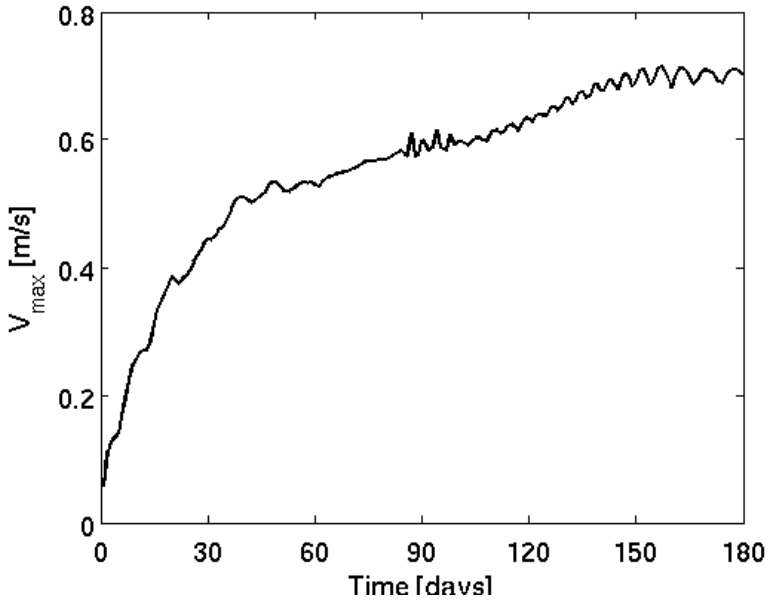

Figure 2.2: The maximum velocities $[\mathrm{m\,s^{-1}}]$ as a function of time in days for B1; Shapiro filter; $A_M = 400\,\mathrm{m^2\,s^{-1}}$

Results

When the horizontal viscosity $A_M = 200\,\mathrm{m^2\,s^{-1}}$ the solution is unstable, but with Shapiro filtering the solution becomes stable. The solution converge without filtering when A_M is approximately $800\,\mathrm{m^2\,s^{-1}}$. (Figure 2.2 for the maximum velocities when $A_M = 400\,\mathrm{m^2\,s^{-1}}$ and filtering is used). An artificial large scale oceanic flow is created. The false geostrophic flow has the largest velocities at the shelf, close to the steep slope, see Figure 2.3 for the velocities $V = \sqrt{u^2 + v^2}$ at 100 m depth.

The numerical results showed that in the ocean basin case the slope parameter r needs to be significantly smaller than 1 for stable results. In the simulations above $r = 0.44$ with Shapiro filtering and $r = 0.71$ without filtering.

By investigating the change in density after a time at a given depth, it is possible to study a density pattern, see Figure 2.4. The interface has risen at the slope, while at the interior the density is lower. Note that the change occurs at the shelf slope. The pattern correlate with a downwelling. This can be observed in Figure 2.5 for the surface elevation.

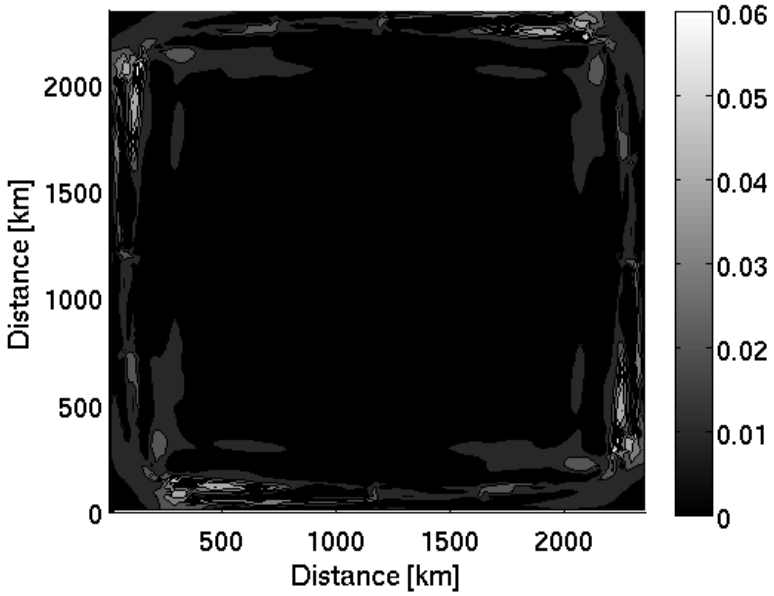

Figure 2.3: The velocities V [$\mathrm{m\,s^{-1}}$] at 100 m depth after 180 days for B1; $A_M = 400\,\mathrm{m^2\,s^{-1}}$

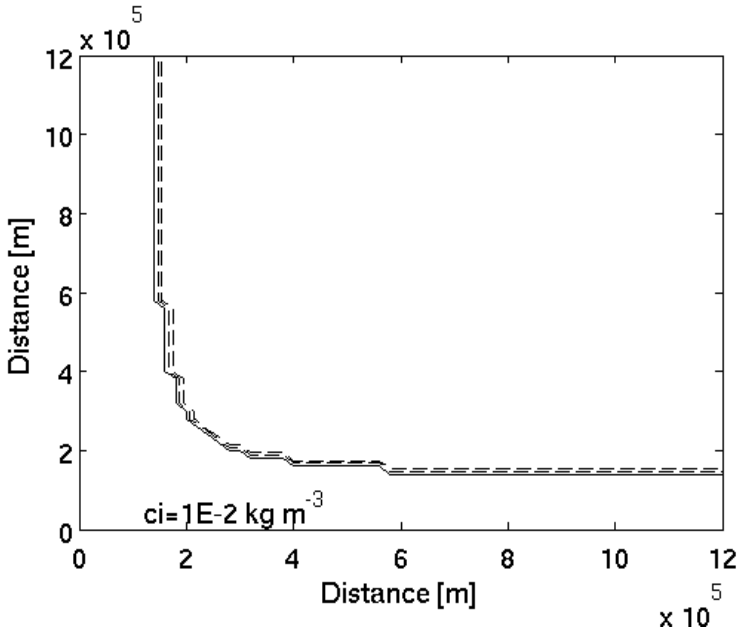

Figure 2.4: The change in density [$\mathrm{kg\,m^{-3}}$], in one corner of B1, at 1000 m depth after 150 days; Solid lines positive change; Dashed negative change; $A_M = 400\,\mathrm{m^2\,s^{-1}}$

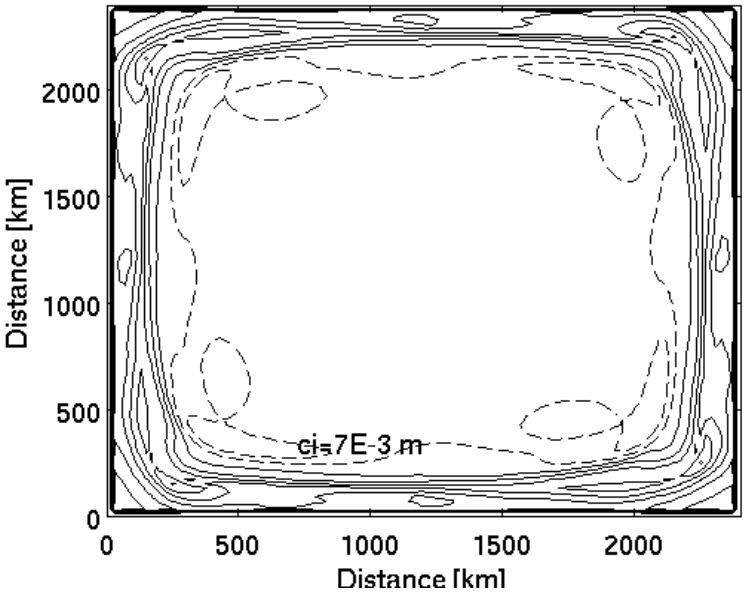

Figure 2.5: The surface elevation [m] after 180 days for B1; Solid lines positive elevation; Dashed negative elevation; $A_M = 400\,\mathrm{m^2\,s^{-1}}$

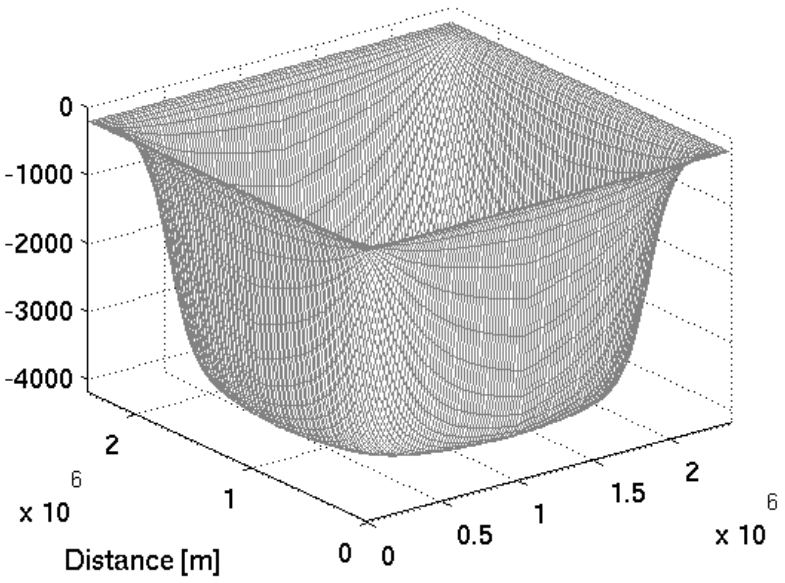

Figure 2.6: The geometry of test basin 2

2.1.2 Basin 2

Bathymetry

The second basin, hereafter referred to as B2, is given by

$$h = h_m + \Delta h \tanh(\frac{d - M}{W}) \ ,$$

where h_m is the depth when $h_0 = 2h_m - h_s$. As above, h_0 is the depth of the deep ocean and h_s is the depth of the continental shelf. Furthermore $\Delta h = h_m - h_s$, d is given as in B1, M is the distance from the closest horizontal boundary at depth h_m to the shelf slope and W is half the width of the slope. By choosing variables so that B1 and B2 have approximately the same bathymetry one get $h_m = 2100\,\mathrm{m}$, $h_s = 200\,\mathrm{m}$, $M = 150\,\mathrm{km}$ and $W = 50\,\mathrm{km}$, see Figure 2.6.

Results

The solution does not reach equilibrium when $A_M = 200\,\mathrm{m^2\,s^{-1}}$, but the maximum velocities are lower than in B1. See Figure 2.7 for the maximum velocities, Figure 2.8 for the velocities $V = \sqrt{u^2 + v^2}$ at 100 m depth, Figure 2.9 for the change in density and Figure 2.10 for the surface elevation. Here $A_M = 400\,\mathrm{m^2\,s^{-1}}$. The main features in the figures are the same as in B1. Given the smooth tanh-function, the slope parameter is small, $r = 0.20$.

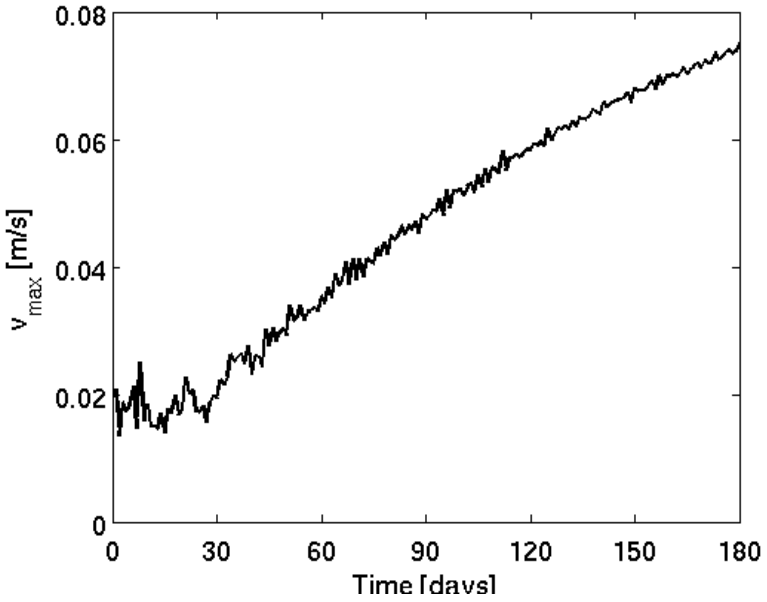

Figure 2.7: The maximum velocities [$\mathrm{m\,s^{-1}}$] as a function of time in days for B2; $A_M = 400\,\mathrm{m^2\,s^{-1}}$

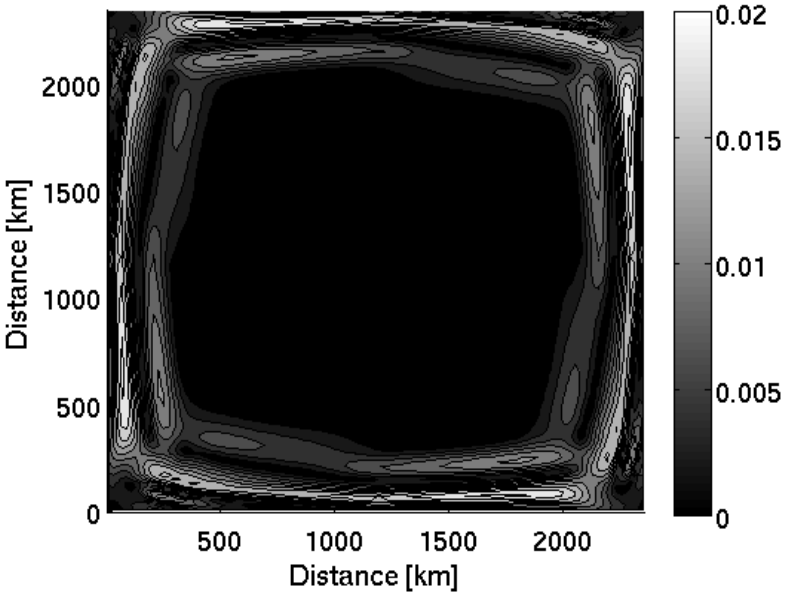

Figure 2.8: The velocities V [$\mathrm{m\,s^{-1}}$] at 100 m depth after 180 days for B2; $A_M = 400\,\mathrm{m^2\,s^{-1}}$

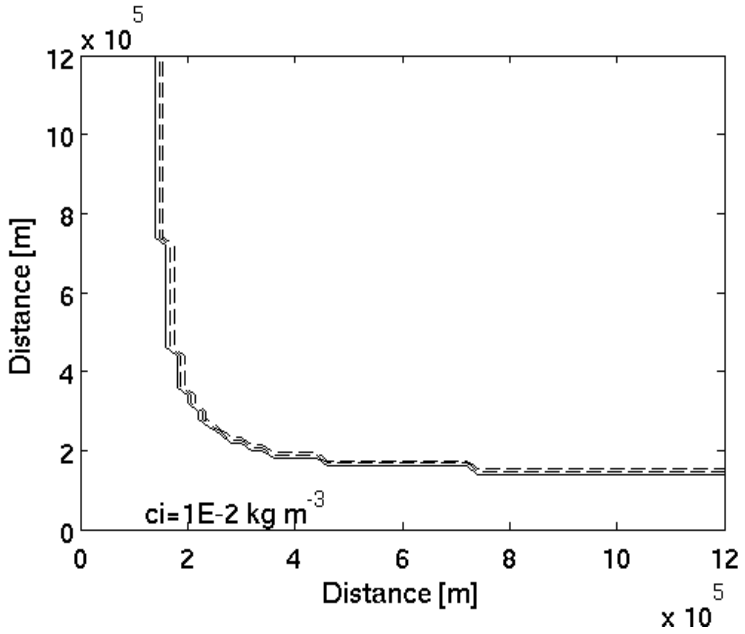

Figure 2.9: The change in density [$\mathrm{kg\,m^{-3}}$], in one corner of B2, at 1000 m after 150 days; Solid lines positive change; Dashed negative change; $A_M = 400\,\mathrm{m^2\,s^{-1}}$

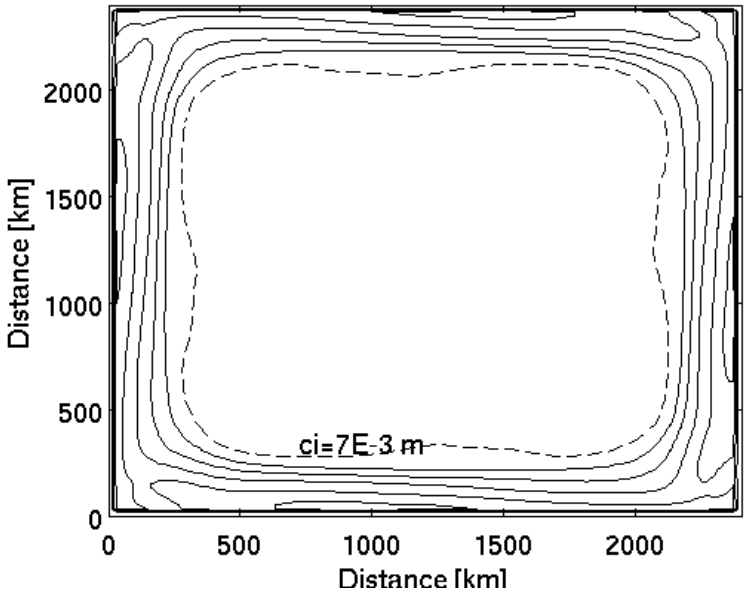

Figure 2.10: The surface elevation [m] after 180 days for B2; Solid lines positive elevation; Dashed negative elevation; $A_M = 400\,\mathrm{m^2\,s^{-1}}$

2.2 Comparing the basins

Both basins have steep topography, which can lead to large errors in the pressure gradient force. The main difference is the smoothness of the curve in B2 compared to the singularity, where the shelf meets the slope, in B1. Also, the slope parameter r in B2 is lower than in B1. These two factors may explain the fact that the maximum velocity in B2, when $A_M = 400\,\mathrm{m^2\,s^{-1}}$ (Figure 2.7), is noticeably lower than in B1 (Figure 2.2). This can also be seen in Figure 2.3 and Figure 2.8 for the computed velocities $V = \sqrt{u^2 + v^2}$ at 100 m. One may question if the maximum velocity in B2 would be the smallest of the two, after a longer run. In Figure 2.2 the velocity seems to reach an equilibrium, while in Figure 2.7 the solution is still growing. The surface elevation (Figure 2.5 and Figure 2.10) and the density difference (Figure 2.4 and Figure 2.9) are of the same magnitude in both basins.

Based on the smaller velocities measured in B2, the smooth basin is chosen for the later experiments.

Chapter 3

Physical phenomena

Realistic test cases try to recapture real physical phenomena. By focusing on one given oceanic motion, in an idealised test case, it is easier to see if the phenomenon is correctly recreated. The physical phenomena experimented on in this chapter are Kelvin waves. They are easy to generate, and the reach and the velocity of the simulated waves are easy to measure and to compare to the real waves.

3.1 External Kelvin waves

Coastal upwelling is often followed by Kelvin waves in nature. A wave is generated because an upwelling is created in one given area along the coast and the system tries to go back to its initial state. The wave needs the lateral boundary to propagate. Its maximum amplitude is found at the coast and the elevation decays further away from the sea shore. If the bottom is flat and the coast is vertical, the reach of the wave depends on the external Rossby radius of deformation R_0. Following Kundu and Cohen [2004]

$$R_0 = \frac{\sqrt{gh}}{f} \ .$$

Here g is the gravity, h is the bottom depth and $f = 10^{-4}\,\mathrm{s}^{-1}$ is the Coriolis parameter. The amplitude decays exponentially away from the boundary with R_0 as the decay scale. With $h = 200\,\mathrm{m}$ at the continental shelf one has $R_0 \approx 443\,\mathrm{km}$. Since the shelves in B1 and B2 are to narrow for displaying the given physical phenomenon, a new basin is designed, B3 (Figure 3.1). B3 is equal to B2, see subsection 2.1.2, but it has a broader shelf, $M = 400\,\mathrm{km}$. The reach of the waves will still be limited by the shelf, but the main features of the phenomenon should be recognised.

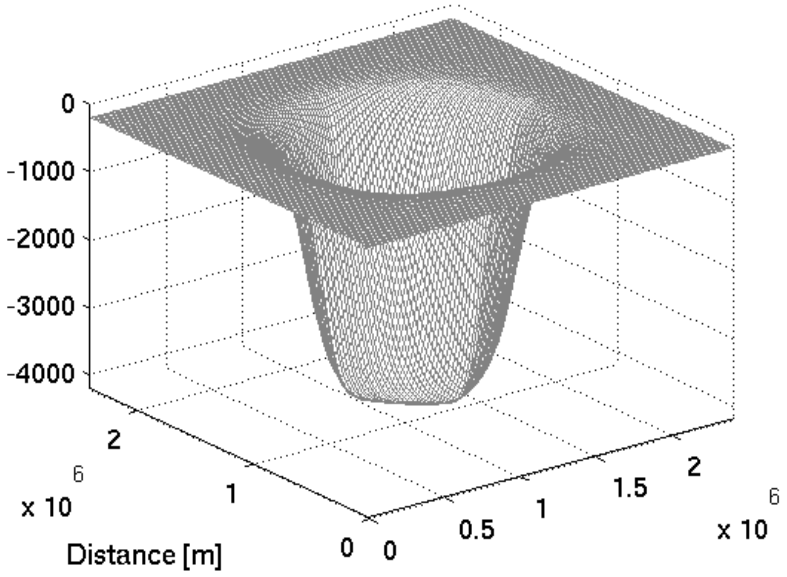

Figure 3.1: The geometry of test basin 3

Notice that it is still unclear if the test case is stable when the horizontal viscosity $A_M = 400\,\mathrm{m^2\,s^{-1}}$ (Figure 3.2). Grid, boundary conditions, initial state, reference stratification ρ_{ref}, perturbation density ρ' and Burger number S are as given in Section 2.1. The slope parameter r is smaller than in the previous cases. Here $r = 0.12$.

To generate the waves, the surface elevation in a square section, ($400\,\mathrm{km} \times 400\,\mathrm{km}$), in the south west corner is raised 1 m initially. The perturbation triggers a wave that is bound to the boundary and travels with the coast to the right, see Figure 3.3. A smaller wave is also seen travelling along the western boundary. The different sizes of the waves can be explained by the Coriolis force. After five hours, the foremost peak of the largest wave, has a reach of 390 km, see Figure 3.3. As assumed, the surface displacement is zero, when the wave has reached the deeper part of the ocean.

By comparing different plots of the wave propagation it is possible to find the velocity c of the wave. In the given case the observed velocity c is approximately equal to the computed velocity $c_0 \approx 161\,\mathrm{km\,h^{-1}}$. The computed velocity c_0 is given in $\mathrm{m\,s^{-1}}$ by

$$c_0 = \sqrt{gh}\ .$$

Here g is the gravity and h is the depth of the continental shelf [Kundu and Cohen, 2004].

One may conclude that the test basin represents external Kelvin waves in a satisfactory manner.

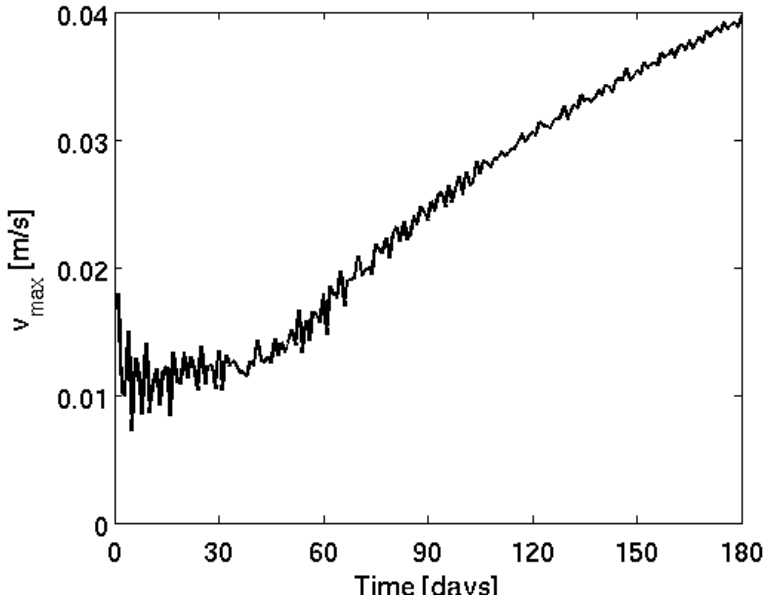

Figure 3.2: The maximum velocities [$\mathrm{m\,s^{-1}}$] as a function of time in days for B3 with exponential stratification; $A_M = 400\,\mathrm{m^2\,s^{-1}}$

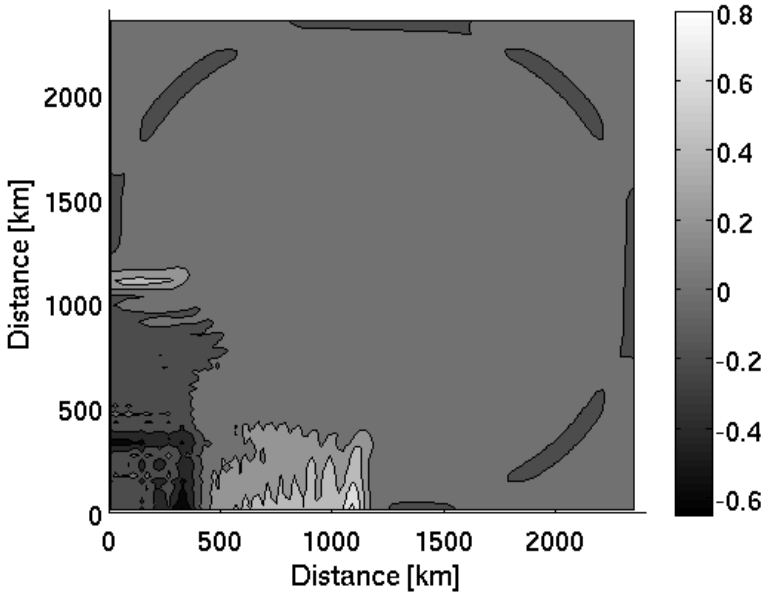

Figure 3.3: The surface elevation [m] after 5 hours for B3. The water elevation is initially raised in one corner; $A_M = 400\,\mathrm{m^2\,s^{-1}}$

3.2 Internal Kelvin waves

Oscillating within the fluid instead of on the surface, internal waves are found everywhere in the ocean. Analogous to the external Kelvin waves, internal waves are gravity waves. They try to restore the hydrostatic equilibrium, when the buoyancy and the gravity force are in balance.

Following Kundu and Cohen [2004], the internal Kelvin waves can travel in any continuously stratified fluid. The waves will propagate with different mode speeds

$$c_n = \frac{Nh}{n\pi} , \qquad n = 1, 2, ... \tag{3.1}$$

Here $N = N(z)$ is the buoyancy frequency, see Equation (2.2) and $h = h(x, y)$ is the depth of the ocean. The corresponding decay scales or the internal Rossby radiuses of deformation are

$$R_n = \frac{c_n}{f} , \qquad n = 1, 2, ...$$

By comparison to the external Rossby radius R_0, the internal radius R_n is small. The internal waves might therefore be difficult to examine. In an attempt to make the waves easier to observe, in the upper part of the ocean basin, the reference density profile ρ_{ref} is changed to

$$\rho_{ref}(z) = 28\,\mathrm{kg\,m^{-3}} - \Delta\rho\frac{3}{4}\left(1 + \tanh\left(\frac{z+M}{W}\right)\right) ,$$

where $\Delta\rho = 3.671\,\mathrm{kg\,m^{-3}}$ as before. Note that the stratification profile can be divided into three parts, a distance $2W$ where the density changes its value and two layers with constant density, one above and one below the interface. The thickness of the two constant layers can be adjusted by M, the distance from the surface to the middle of the layer where ρ_{ref} changes its value. Here $W = 250\,\mathrm{m}$ and $M = 100\,\mathrm{m}$. The initial perturbation ρ' is altered to

$$\rho'(z) = -1.5\,\mathrm{kg\,m^{-3}}\,\frac{3}{4}\left(1 + \tanh\left(\frac{z+M}{W}\right)\right) ,$$

see Figure 3.4 for the different density profiles.

By comparing the new buoyancy frequency with the old (Figure 3.5) it is observed that the frequency N has increased in the upper part of the basin.

Figure 3.6 shows that the solution has not reached equilibrium and that the magnitude of the maximum velocities are reasonably low. It is also evident that the maximum velocities oscillate. The oscillations are investigated further in Subsection 4.2.1.

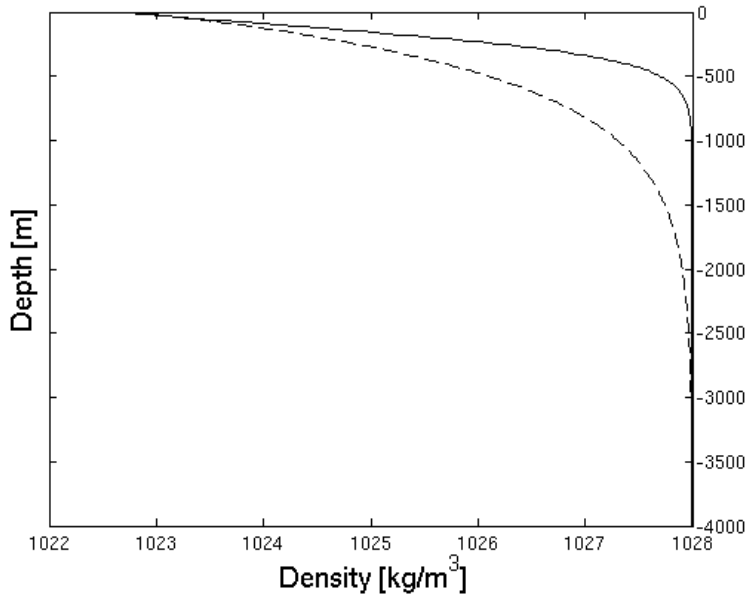

Figure 3.4: The vertical distribution of density [$\mathrm{kg\,m^{-3}}$]; Solid lines tanh profile; Dashed exponential profile

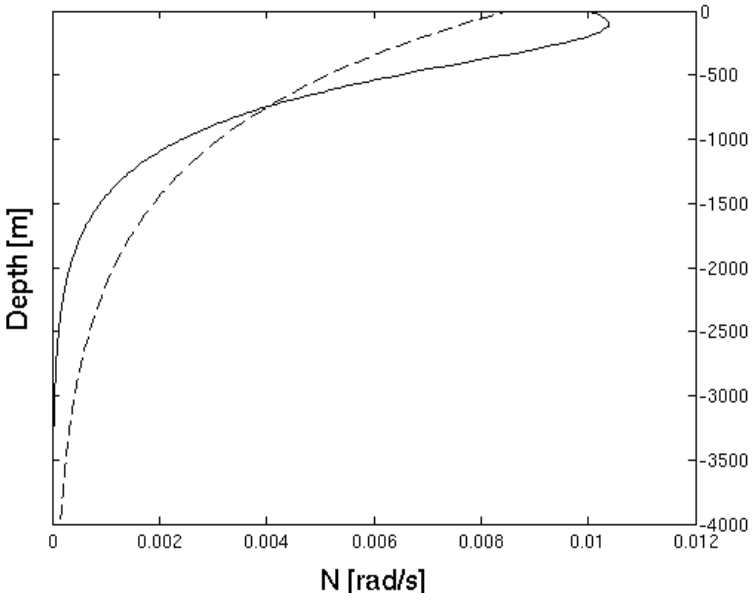

Figure 3.5: The vertical distribution of the buoyancy frequency [$\mathrm{rad\,s^{-1}}$]; Solid lines tanh density profile; Dashed exponential density profile

For $n = 1$ at the shelf ($h = 200\,\mathrm{m}$) and with $N \approx 1.04 \cdot 10^{-2}\,\mathrm{rad\,s^{-1}}$, the internal Rossby radius R_1 is approximately 6620 m at 100 m depth. Since the grid resolution is too large (20 km), the waves will not be represented with the present grid. To observe a wave, the internal Rossby radius needs to be greater than $2\Delta x$ or 40 km. This can be done by reducing the Coriolis parameter f or increasing the buoyancy frequency N.

In the deep part of the ocean ($h = 4000\,\mathrm{m}$), $R_1 \approx 132\,\mathrm{km}$. Internal Kelvin waves can therefore be observed in the test case, but only travelling along the shelf slope. Since the equations above are valid for waves travelling along a straight coast, vertically on a horizontal bottom, the phenomenon observed and the equations may not correlate.

Internal motions stand for most of the internal mixing in the ocean [Bergh, 2010]. If there is no deep mixing, the ocean will after a time have no flow below a shallow upper layer [Munk and Wunsch, 1998]. It is therefore important for ocean models to be able to represent oscillations and internal waves. Here the model's ability to represent internal waves is tested by changing the Coriolis parameter f.

In Figure 3.7 the density in a square section (80 km × 80 km), in the south west corner is reduced by $0.01\,\mathrm{kg\,m^{-3}}$. The Coriolis parameter f is also reduced to $10^{-5}\,\mathrm{s^{-1}}$. A wave is generated that travels eastward. It is difficult to measure the exact mode speed and the reach of the wave. At times, the wave front pauses and sometimes it even travels to the west. If the wave speed is calculated from the observed wave fronts after 1 day and 30 days, one get $c \approx 0.29\,\mathrm{km\,h^{-1}}$. The corresponding internal Rossby radius R and mode n are approximately 8 km and 8.3, respectively. Note that n is not an integer and that the internal Rossby radius is less then $2\Delta x$ (40 km). The radius is also not representative for the reach of the wave observed in Figure 3.7, where $R \approx 30\,\mathrm{km}$. Observe that the mode speed is lower than the external mode speed c_0. The solution is unstable, due to the perturbed stratification, see Figure 3.8. Accordingly, the investigation of the internal Kelvin waves will not be addressed further in this thesis.

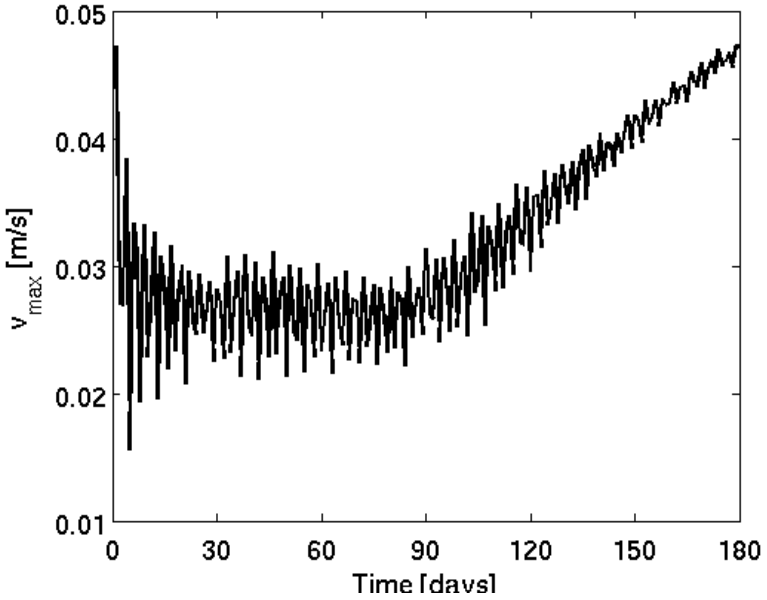

Figure 3.6: The maximum velocities [$\mathrm{m\,s^{-1}}$] as a function of time in days for B3 with tanh stratification; $A_M = 400\,\mathrm{m^2\,s^{-1}}$

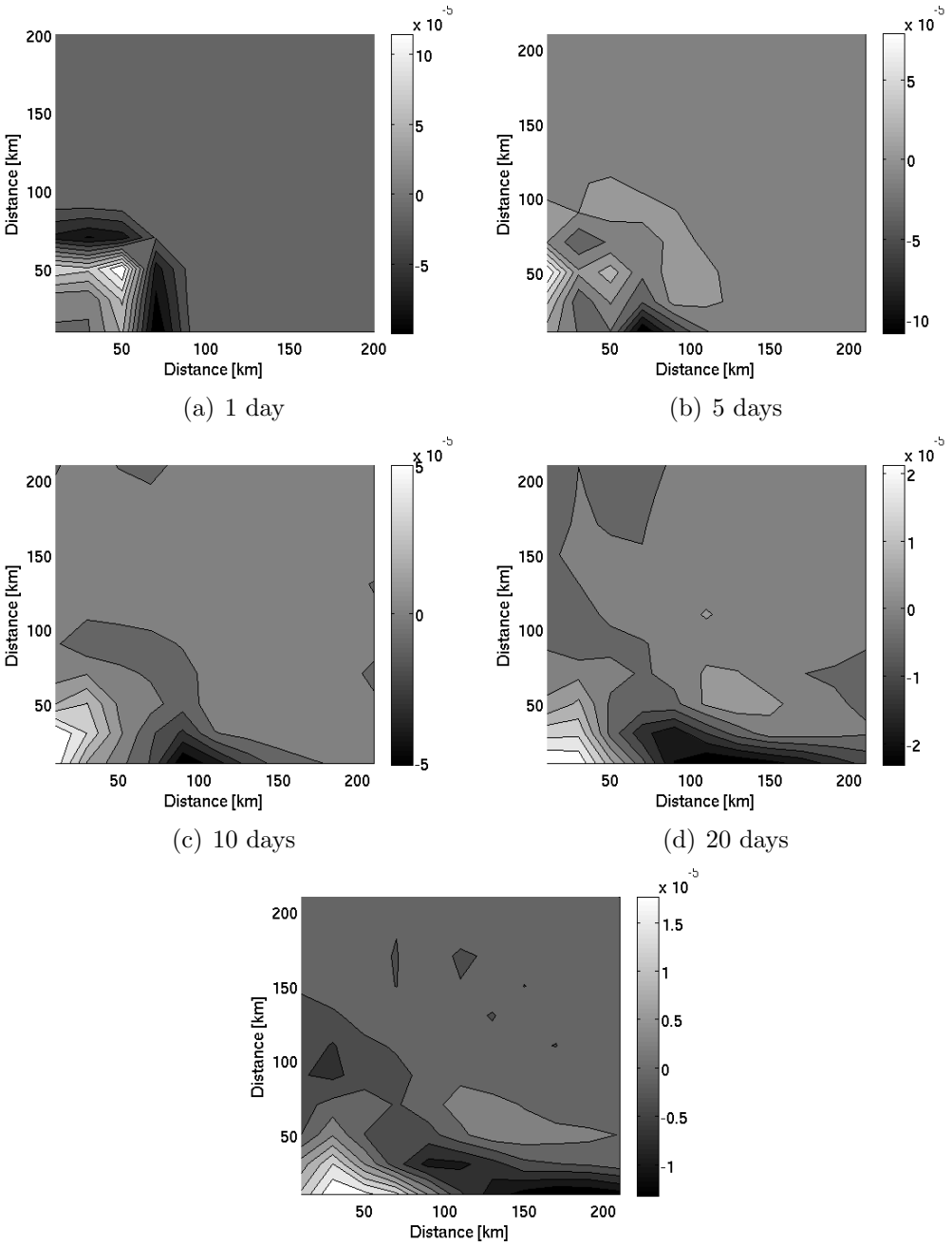

(a) 1 day

(b) 5 days

(c) 10 days

(d) 20 days

(e) 30 days

Figure 3.7: The vertical velocities $[\mathrm{m\,s^{-1}}]$ in one part of B3. In one corner, the tanh stratification is perturbed; $A_M = 400\,\mathrm{m^2\,s^{-1}}$

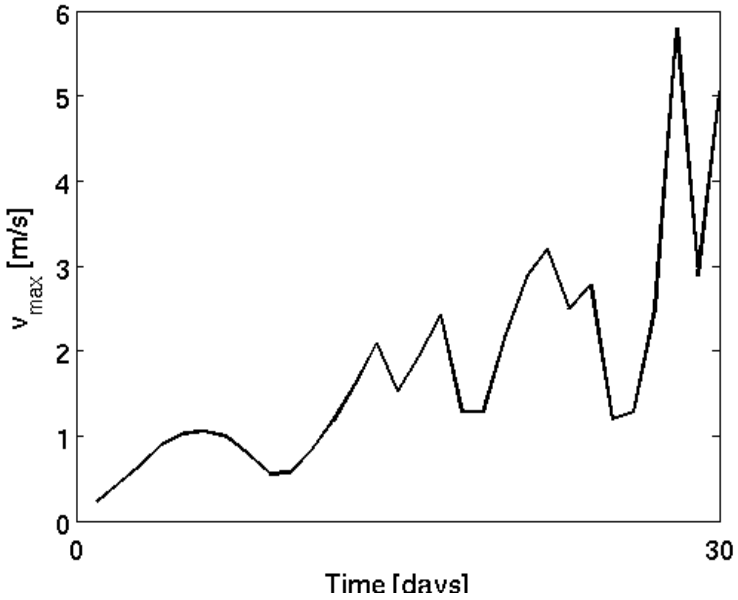

Figure 3.8: The maximum velocities $[\mathrm{m\,s^{-1}}]$ as a function of time in days for B3. In one corner, the tanh stratification is perturbed; $A_M = 400\,\mathrm{m^2\,s^{-1}}$

Chapter 4

Sigma errors

Mellor et al. [1998] identified two types of sigma errors. The first (SEFK) vanished due to the advection of the density field, while the second (SESK) was found to be small. They connected the SESK to the vorticity. In the seamount case, the initial SESK can be observed as an eight-lobe pattern.

4.1 Vorticity errors

In the present study, the internal pressure gradient errors in basins are investigated. By comparison to the seamount case, which has a peak appearing in the middle of the ocean (Figure 4.1), the basins have a depression. Investigating the initial vorticity errors for B3, with tanh stratification, shows that the model reacts differently to the formations. In Figure 4.2 the field of the initial acceleration of the vertically integrated vorticity

$$\frac{\partial}{\partial t}\int_{-1}^{0}\left(\frac{\partial v}{\partial x}-\frac{\partial u}{\partial y}\right)d\sigma \ ,$$

is shown. The sixteen vortices, eight positive and eight negative, are situated near the steep topography and appear in pairs. The difference in the curvature may be the reason for the more circular and outspread vortices in the seamount case (i.e. Figure 4.3 when the standard second order POM method is used). The positions of the vortices on the circular shelf may be a consequence of the grid rotation or the fact that B3 has the steepest slopes at the given locations. The main features are the same when changing between exponential and tanh stratification. Note that the setup from Shchepetkin and McWilliams [2003] is used, when figures from the seamount test case are presented.

The field of the initial acceleration of the vertically integrated vorticity in the seamount test case, was observed as an eight-lobe pattern around the

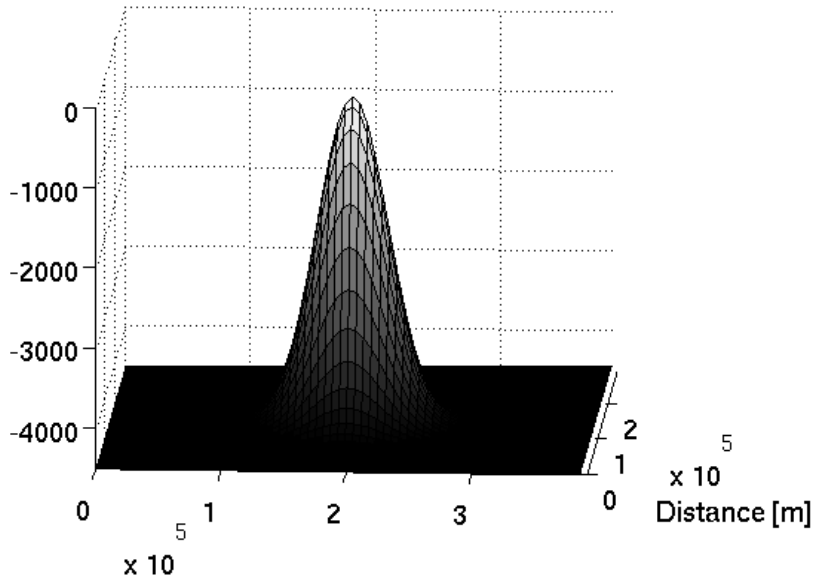

Figure 4.1: The seamount

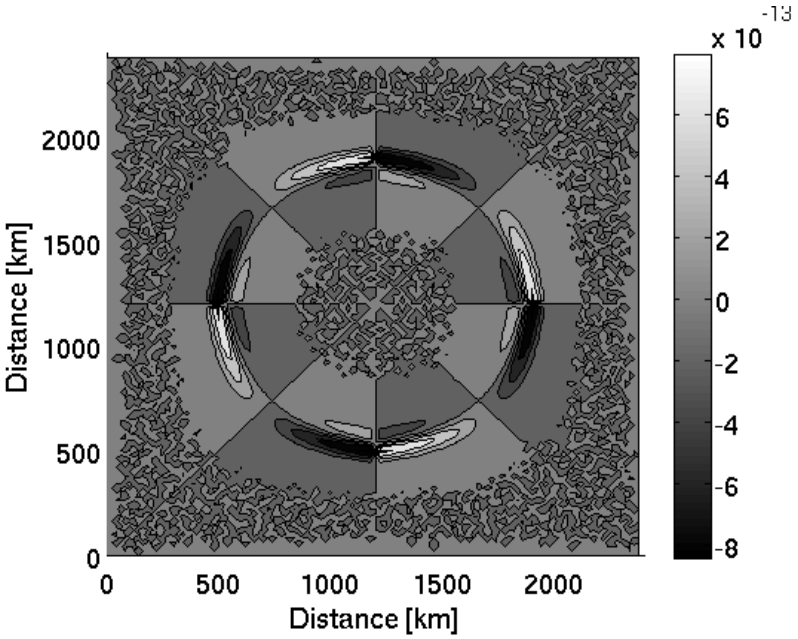

Figure 4.2: The initial acceleration of the vertical integrated vortices [$\mathrm{m\,s^{-2}}$] in B3 with tanh stratification; $A_M = 400\,\mathrm{m^2\,s^{-1}}$

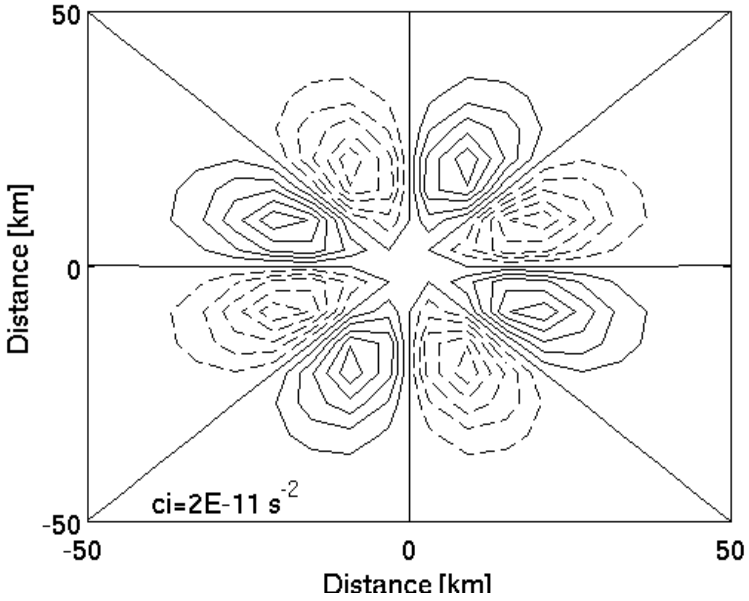

Figure 4.3: The initial acceleration of the vertically integrated vortices [$\mathrm{m\,s^{-2}}$] for the seamount;

seamount (Figure 4.3). Berntsen [2002] found that the pattern changed in time, if the Smagorinsky-type viscosities used not were approximately 100 times larger then recommended. The phenomenon was explained by the fact that there has to be a balance between the centrifugal and the Coriolis force. A dimensionless number, the Rossby number R_O, is normally used to investigate the influence of the two different forces on the system. The Rossby number is given by

$$R_O = \frac{U}{Kf} \ ,$$

where U and K are, respectively, the characteristic velocity and length scale of the phenomenon. If there is an approximate balance, the length scales of the eddies have to increase analogous with the velocities. The vortices then interact to create a new pattern. By observing the vorticity at different times in B3, one notices that the vortices always are present and that they continue to appear in the north, east, south and west of the shelf slope, see Figure 4.4. Due to conservation of potential vorticity, the vortices follow isolines of the bathymetry. Also here the number of vortices change in time. In B3 there is sometimes one pair of vortices in one position (Figure 4.4(a)), but at other times there are several pairs (Figures 4.4(d)). Additionally, some vortices seem to depart from the main formations and travel counter clockwise before disappearing, see 4.4(b). After a time the pattern seem to stay fixed (Figure 4.4(e)).

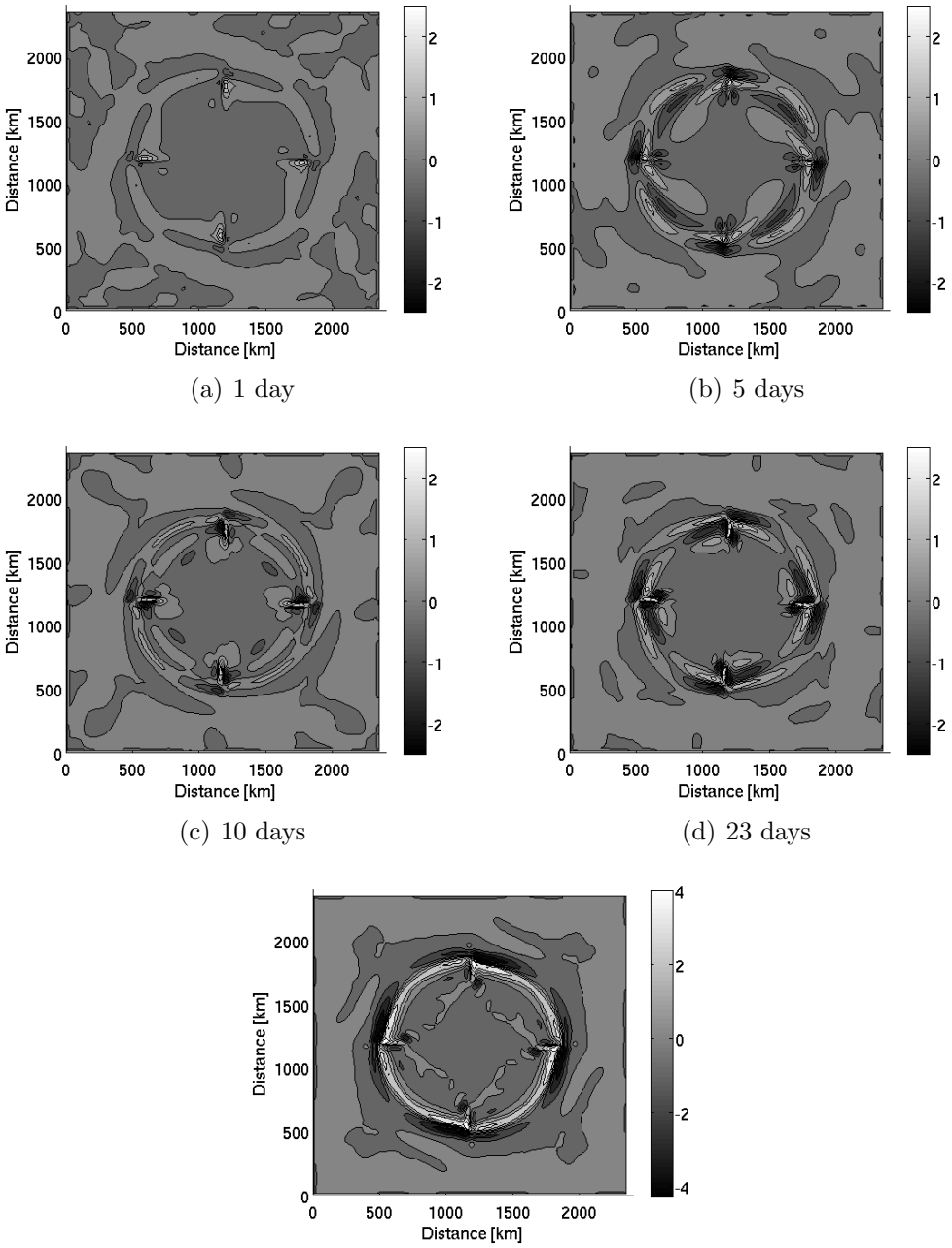

(a) 1 day

(b) 5 days

(c) 10 days

(d) 23 days

(e) 150 days

Figure 4.4: The vertical integrated vorticity [$\mathrm{m\,s^{-1}}$] in B3 with tanh stratification; $A_M = 400\,\mathrm{m^2\,s^{-1}}$

4.2 New errors

When investigating internal waves, a new stratification profile was introduced, see Section 3.2. The figure of the maximum velocities (Figure 3.6) showed large oscillations. Accordingly, one may investigate the vertical velocity.

4.2.1 Vertical velocity

An examination of the vertical velocity at 100 m below the surface after 10 days, reveals a circular pattern situated above the steep slope. In the centre the vertical velocities differ from zero, see Figure 4.5. The circle is made up of many small formations that are approximately $2\Delta x$ long and Δx wide (Figure 4.6). The artificial velocities oscillate with an almost constant period, $T \lesssim \frac{2\pi}{f}$ s, in the small formations, see Figure 4.7. The circular frequency ω of the oscillations is approximately $1.09 \cdot 10^{-4}\,\mathrm{rad\,s^{-1}}$. By comparing ω to the Coriolis parameter $f = 10^{-4}\,\mathrm{s^{-1}}$, one observes that they are almost equal. Following Kundu and Cohen [2004] internal waves are only found when ω is in the frequency range

$$f < \omega < N,$$

where it is assumed that $N > f$. By investigating Figure 3.5, one can observe that the last inequality is fulfilled at least in the upper half of the basin. Note

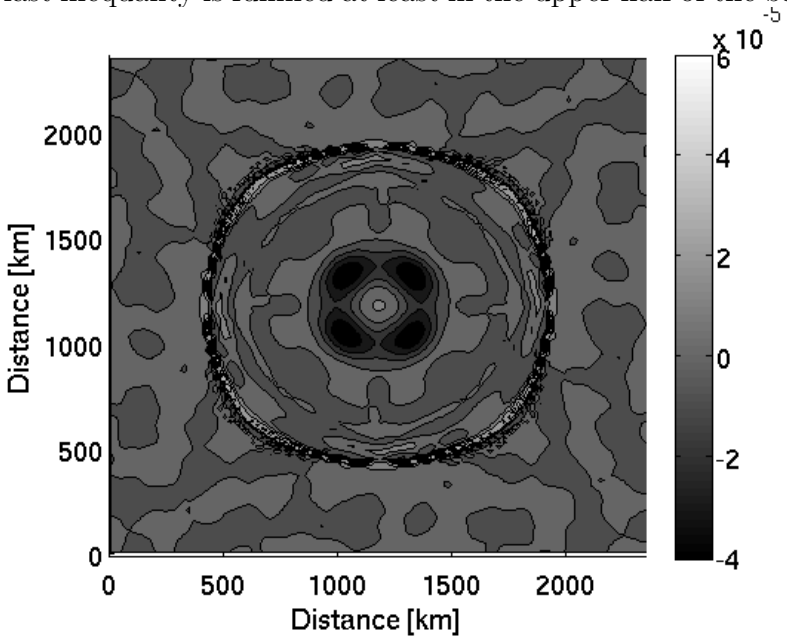

Figure 4.5: The vertical velocities $[\mathrm{m\,s^{-1}}]$ at 100 m depth after 10 days in B3 with tanh stratification; $A_M = 400\,\mathrm{m^2\,s^{-1}}$

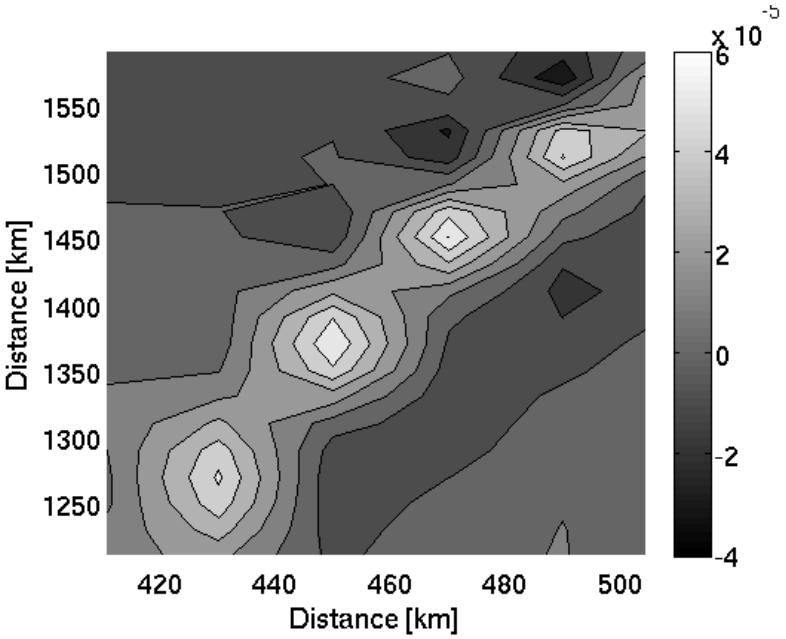

Figure 4.6: The vertical velocities [$\mathrm{m\,s^{-1}}$] at 100 m depth after 10 days in one part of B3 with tanh stratification; $A_M = 400\,\mathrm{m^2\,s^{-1}}$

that the circular frequency ω lie in the range. For this reason, it should be possible to find internal waves in the oceanic basin.

It is reasonable to assume that the artificial density perturbation, created by the internal pressure gradient, generate gravity waves. After a time, it may be possible to observe that the waves are affected by the Coriolis force. The force can create a phenomena travelling counter clockwise around the basin.

By investigating the pattern at different times it is observed that the large circle, around the basin (Figure 4.5), always consists of the small formations. The noise may be a consequence of the leapfrog scheme used in the model (see Chapter 5). This scheme is known to be too dispersive. As revealed by Figure 4.7, the vertical velocities in the formation oscillate. In contrast to the circle, the pattern in the centre change in time (The four surrounding circles may e.g. disappear and the circle in the centre expand, see Figure 4.8). After a time, a new formation in the pattern is evident. Situated just inside the circle, in the north, east, south and west, the pattern shows four spikes directed to the centre of the circle, see Figure 4.8. A similar phenomenon was observed when the vorticity was investigated (Section 4.1) and will be found when studying the initial acceleration of the horizontal divergence (Subsection 4.2.2), the horizontal advection of the density field (Subsection 4.2.3), the density diffusion (Section 4.3), the upwind scheme

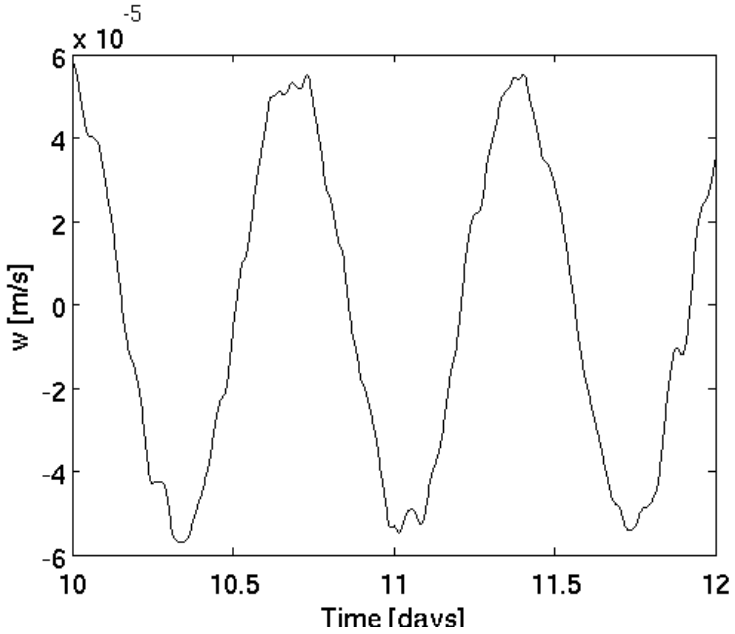

Figure 4.7: The vertical velocities [$\mathrm{m\,s^{-1}}$] as a function of time in days for B3 with tanh stratification, in the cell situated at (450 km,1370 km) at 100 m depth; $A_M = 400\,\mathrm{m^2\,s^{-1}}$

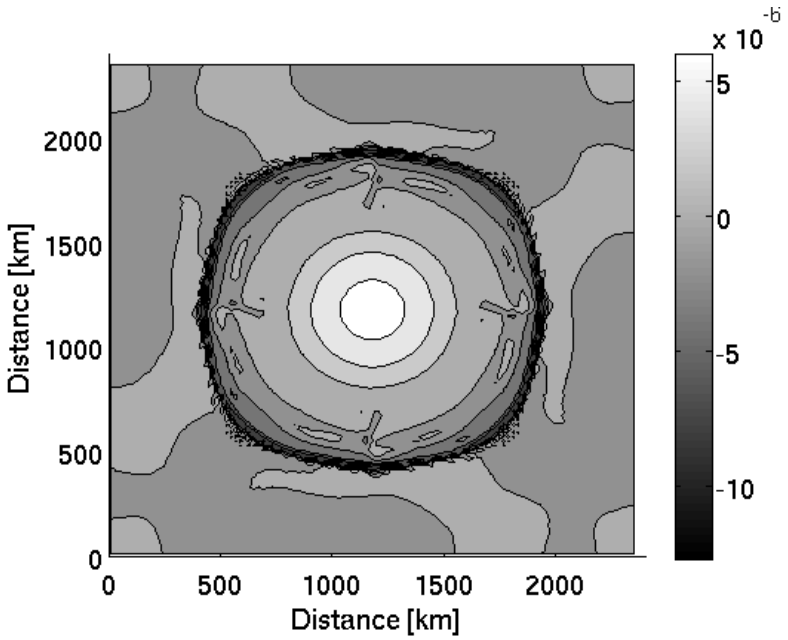

Figure 4.8: The vertical velocities [$\mathrm{m\,s^{-1}}$] at 100 m depth after 150 days in B3 with tanh stratification; $A_M = 400\,\mathrm{m^2\,s^{-1}}$

(Section 5.1) and the TVD scheme (Section 5.2). Note that the spike in the south inclines to the right as a consequence of the Coriolis force. The other spikes lean accordingly.

If the Coriolis parameter f is changed to $10^{-5}\,\mathrm{s}^{-1}$, internal waves can be observed in the basin, see Figure 4.9. The front is propagating with an almost constant speed $c = 3.3\,\mathrm{km\,h}^{-1}$, before the wave dissolves. In Section 3.2, an equation for mode speeds of internal Kelvin waves was given, see Equation (3.1). For the first baroclinic mode $c_1 \approx 3.7\,\mathrm{km\,h}^{-1}$ when $h = 4000\,\mathrm{m}$ and $N \approx 1.04 \cdot 10^{-2}\,\mathrm{rad\,s}^{-1}$ at $z = 100\,\mathrm{m}$ depth. Note that the calculated speed c_1 and the observed c have approximately the same magnitude.

Convergence and divergence cause the water to rise and fall. In accordance with Figure 4.7, there has to be a corresponding divergence. One might be tempted to speculate that the oscillations are connected to divergence errors. Also the plot of the vertical velocity (Figure 4.6) shows an interesting phenomenon. It would be reasonable to believe that the noise in the plot should disappear due to advection of density in the horizontal direction. Two experiments, in the following sections, investigate the speculations above.

4.2.2 The initial acceleration of the horizontal divergence

The initial acceleration of the horizontal divergence may give a good indication to why the vertical velocity field observed is created (Figure 4.5). At the beginning of the computations, estimates of the pressure forces $-\frac{1}{\rho_0}\frac{\partial p}{\partial x}$ in the x-direction and the forces $-\frac{1}{\rho_0}\frac{\partial p}{\partial y}$ in the y-direction are calculated and taken as the accelerations $\frac{\partial u}{\partial t}$ and $\frac{\partial v}{\partial t}$, respectively. This allows an easy evaluation of the initial acceleration of the vertically integrated horizontal divergence

$$\frac{\partial}{\partial t}\int_{-1}^{0}\left(\frac{\partial u}{\partial x}+\frac{\partial v}{\partial y}\right)d\sigma\ .$$

A plot of the acceleration is seen in Figure 4.10. By comparing the plot to Figure 4.5 one can see that both patterns display a ring placed near the steep topography. While the main features are the same, the details in the patterns differ. The plot of the vertical velocity field consists of several smaller formations while the plot of the initial acceleration of the horizontal divergence only has four crests situated in the north, east, south and west of the shelf slope. By comparing Figure 4.8 of the vertical velocities after 150 days and Figure 4.10 of the initial acceleration of the vertically integrated horizontal divergence one observes that the spikes and the crests are located

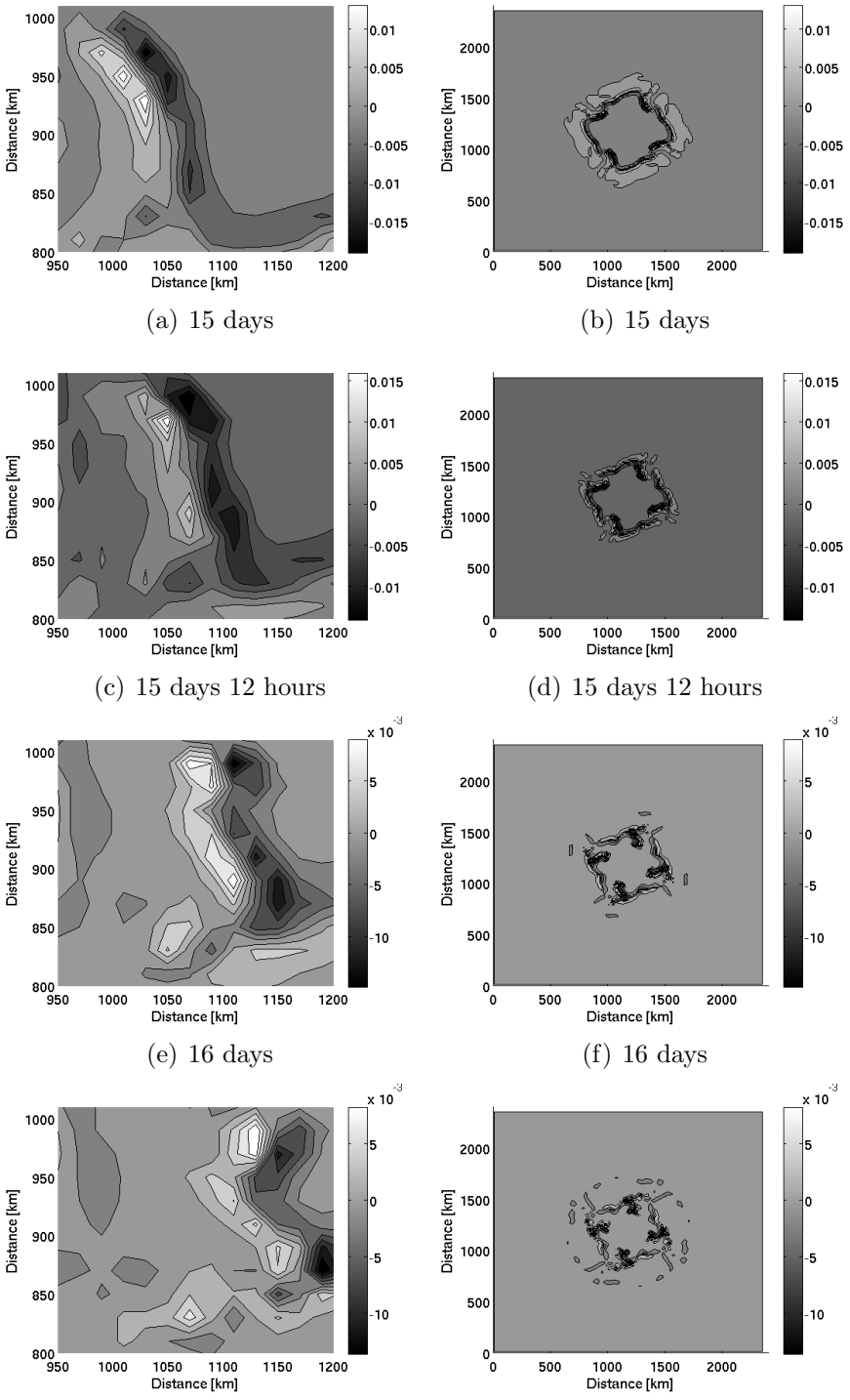

(a) 15 days (b) 15 days

(c) 15 days 12 hours (d) 15 days 12 hours

(e) 16 days (f) 16 days

(g) 16 days 12 hours (h) 16 days 12 hours

Figure 4.9: The vertical velocities [$\mathrm{m\,s^{-1}}$] at 100 m depth in B3 with tanh stratification. The Coriolis parameter $f = 10^{-5}\,\mathrm{s^{-1}}$; $A_M = 400\,\mathrm{m^2\,s^{-1}}$

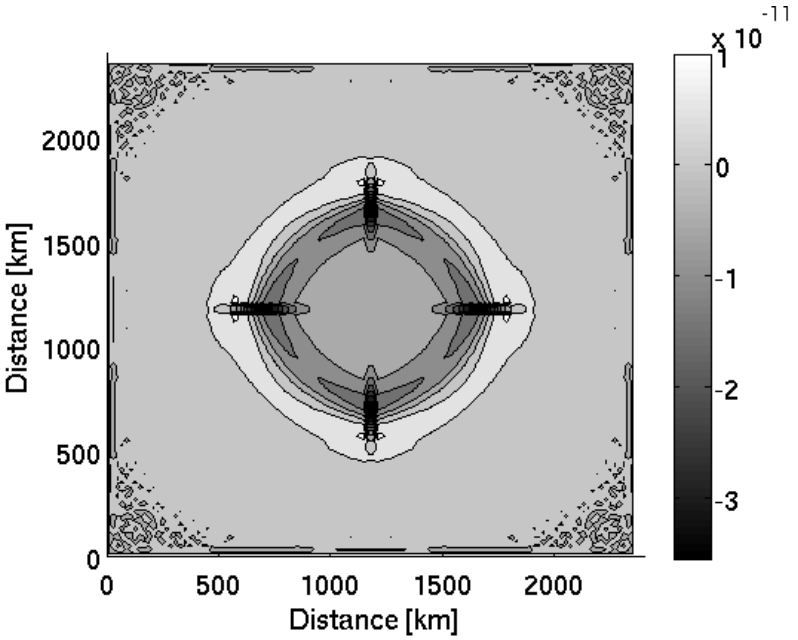

Figure 4.10: The initial acceleration of the vertical integrated horizontal divergences [$\mathrm{m\,s^{-2}}$] in B3 with tanh stratification; $A_M = 400\,\mathrm{m^2\,s^{-1}}$

at the same positions. Mellor et al. [1998] used the same approach to study the vorticity error.

Note that the accelerations are estimated with internal pressure gradients. Errors in the gradients may be transferred to the divergence and cause the formation of the pattern observed in Figure 4.5.

A change in baroclinic pressure gradients can be expressed analytically by combining Equation (1.3) and Equation (1.4)

$$\frac{\partial}{\partial t}\left(\frac{\partial u}{\partial x}+\frac{\partial v}{\partial y}\right)+f\left(\frac{\partial u}{\partial y}-\frac{\partial v}{\partial x}\right)=-\frac{1}{\rho_0}\left(\frac{\partial^2 p}{\partial x^2}+\frac{\partial^2 p}{\partial y^2}\right)+\frac{\partial F_x}{\partial x}+\frac{\partial F_y}{\partial y}\ .$$

Observe that the first term contains an expression for the horizontal divergence, while the second term contains the vorticity. Due to the changes in the pressure gradients there has to be a change in one or more of the other terms in the expression. The equation may explain why it is reasonable to think that there are at least two types of errors connected to 3D flow. One connected to vorticity and one to divergence.

4.2.3 The horizontal advection of the density field

In Chapter 1 the underlying equations in the model were introduced. Several approximations were used to simplify the equations. As a consequence, the model will reduce some of its accuracy. Here the focus will be on the importance of horizontal advection of the density field

$$u\frac{\partial \rho}{\partial x} + v\frac{\partial \rho}{\partial y} \ .$$

The advection was removed when the density derivative $\frac{D\rho}{Dt}$ was linearised, see Sections 1.2 and 1.3. The flow's ability to smooth out the density differences in the horizontal direction is therefore reduced. The equation $\frac{D\rho}{Dt} = 0$ expresses incompressibility of a fluid particle [Kundu and Cohen, 2004].

Figure 4.11 shows that the maximum velocities oscillate with a varying amplitude. The solution still does not reach an equilibrium. The small formations in the circle, in the plot of the vertical velocities, have been reduced, see Figure 4.12(a) and Figure 4.13.

By investigating the vertical velocity field at different times one notices that there are waves going in toward the centre of the basin. The circular waves are generated near the shelf, see Figure 4.12. The period of the waves

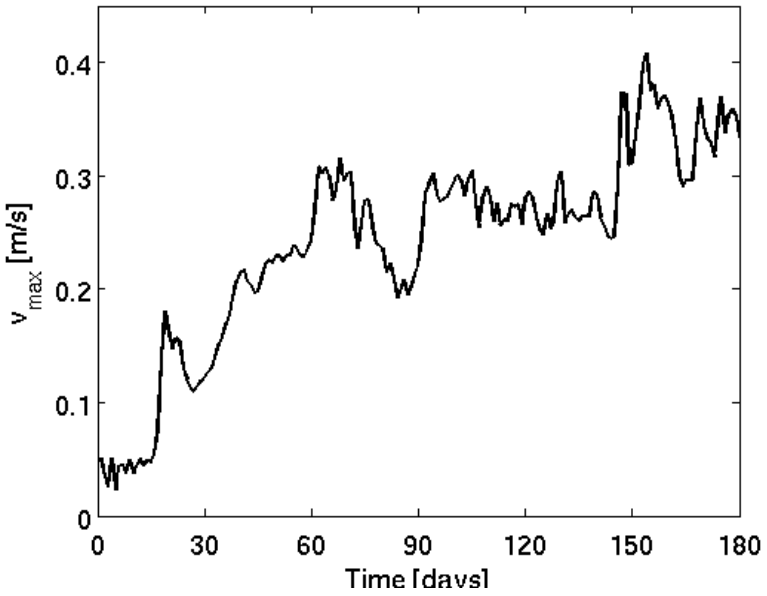

Figure 4.11: The maximum velocities [$\mathrm{m\,s^{-1}}$] depth as a function of time in days for B3 with tanh stratification. The horizontal advection of the density filed is included; $A_M = 400\,\mathrm{m^2\,s^{-1}}$

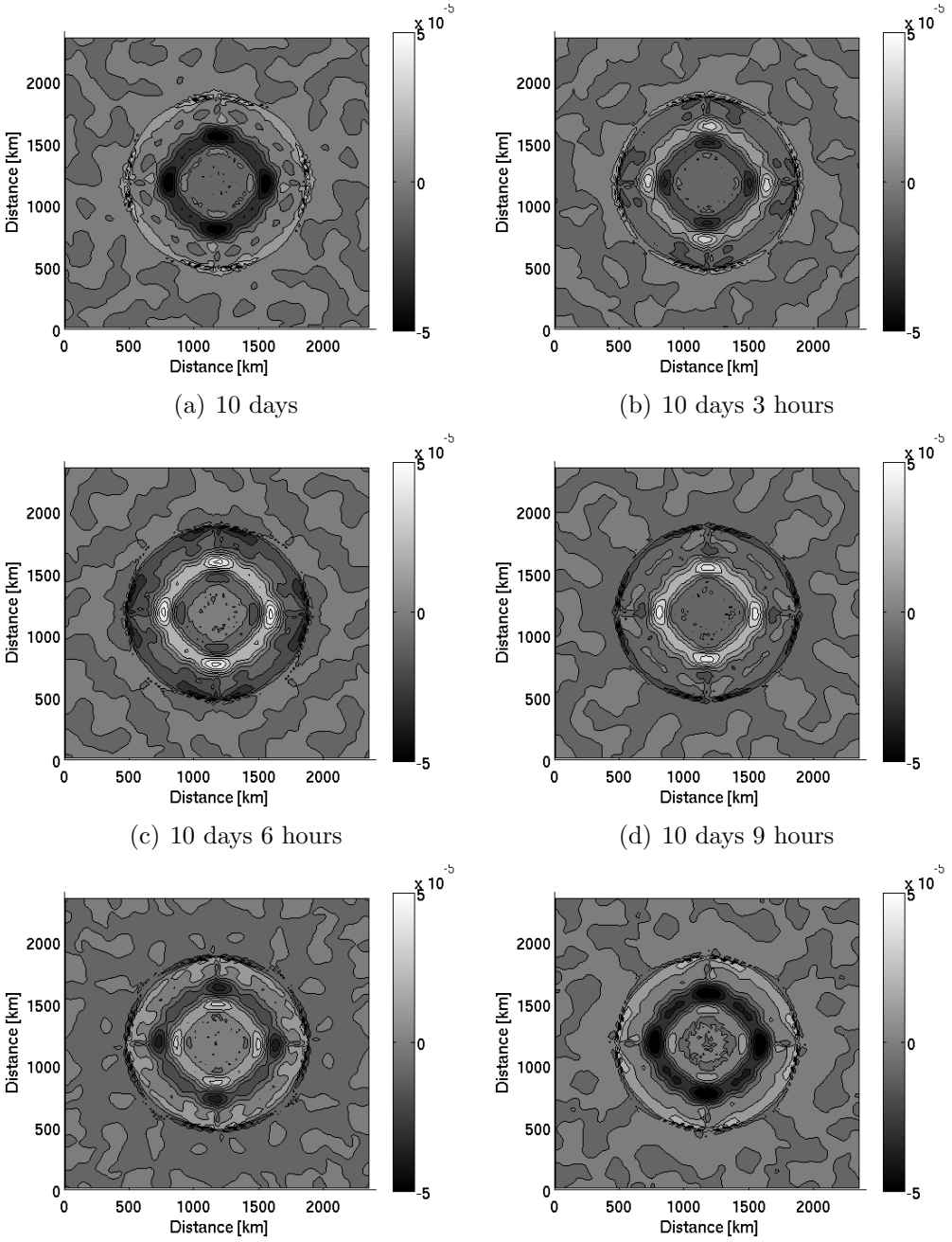

(a) 10 days

(b) 10 days 3 hours

(c) 10 days 6 hours

(d) 10 days 9 hours

(e) 10 days 12 hours

(f) 10 days 15 hours

Figure 4.12: The vertical velocities [$\mathrm{m\,s^{-1}}$] at 100 m depth in B3 with tanh stratification. The horizontal advection of the density field is included; $A_M = 400\,\mathrm{m^2\,s^{-1}}$

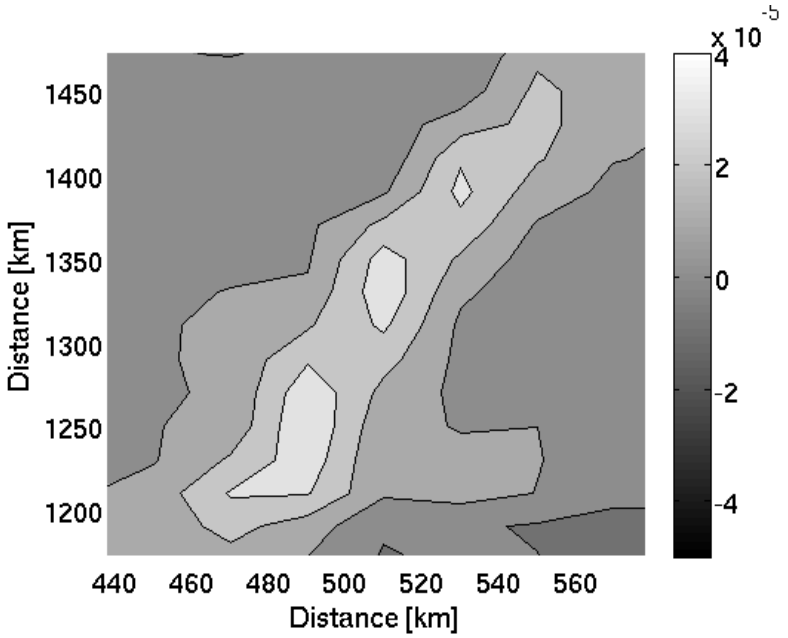

Figure 4.13: The vertical velocities [$\mathrm{m\,s^{-1}}$] at 100 m depth in B3 with tanh stratification. The horizontal advection of the density field is included; $A_M = 400\,\mathrm{m^2\,s^{-1}}$

can be observed in Figure 4.14. Notice that the same period ($T \lesssim \frac{2\pi}{f}$ s) was found in Subsection 4.2.1, when the vertical velocities were studied. It is also worth noticing that the most distinctive features are found in the north, east, south and west as in the other tests in this chapter. The waves may be generated because of the density displacement. Due to the internal pressure gradient errors, the density field close to the steep bathymetry is disturbed. As the gravity and the buoyancy forces try to restore the balance, a wave is created. The shelf slopes toward the centre, this may be the reason why the waves do not travel out to the boundaries.

Later the pattern develops small square formations that are Δx long, see Figures 4.15 and 4.16. The formations are a result of the nonlinearity of the equations. Contrarily to the linear model, the flow of energy is now transported from lower to higher wave numbers. While this may be true for small k, the flow of energy do not continue past a maximum wave number k_{max}. In nature the limit k_{max} does not exist and the transport of energy continues past k_{max}. When the waves get to small in the model, the wave numbers may be "reflected" back on smaller values of k [Haidvogel and Beckmann, 1999]. For this reason, smaller waves may be interpreted as resolvable waves. Note that the model can, due to the finite grid, only resolve waves with wave length longer or equal then $2\Delta x$. The corresponding k_{max} is $\frac{\pi}{\Delta x}$. The noise

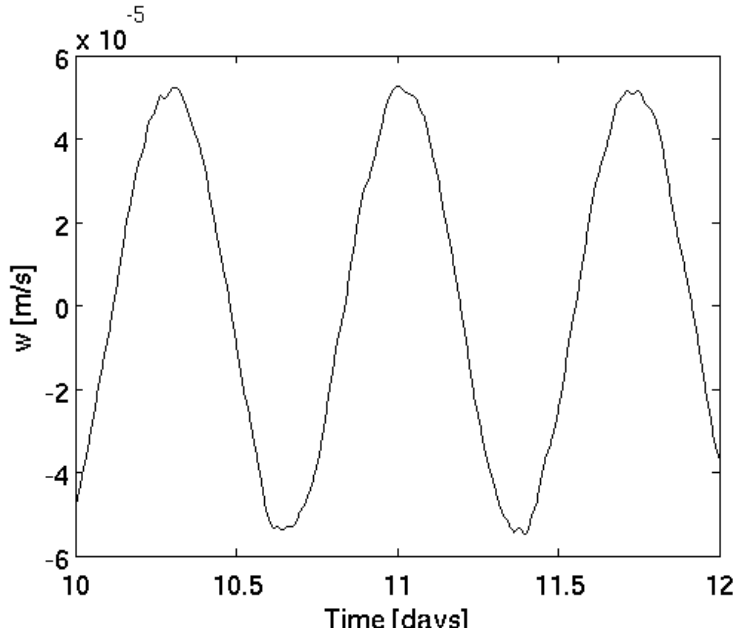

Figure 4.14: The vertical velocities [$\mathrm{m\,s^{-1}}$] as a function of time in days for B3 with tanh stratification, in the cell situated at (790 km,1190 km) at 100 m depth. The horizontal advection of the density field is included; $A_M = 400\,\mathrm{m^2\,s^{-1}}$

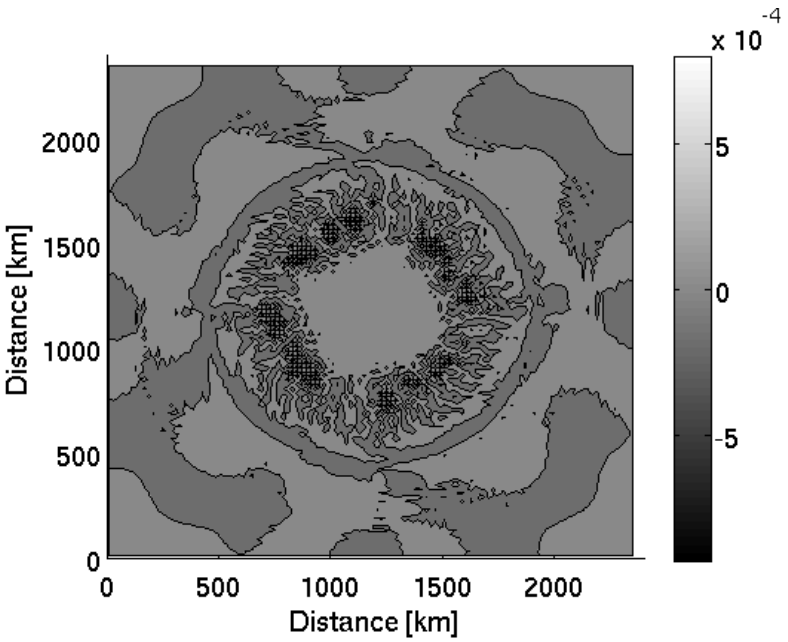

Figure 4.15: The vertical velocities [$\mathrm{m\,s^{-1}}$] at 100 m depth after 150 days in B3 with tanh stratification. The horizontal advection of the density field is included; $A_M = 400\,\mathrm{m^2\,s^{-1}}$

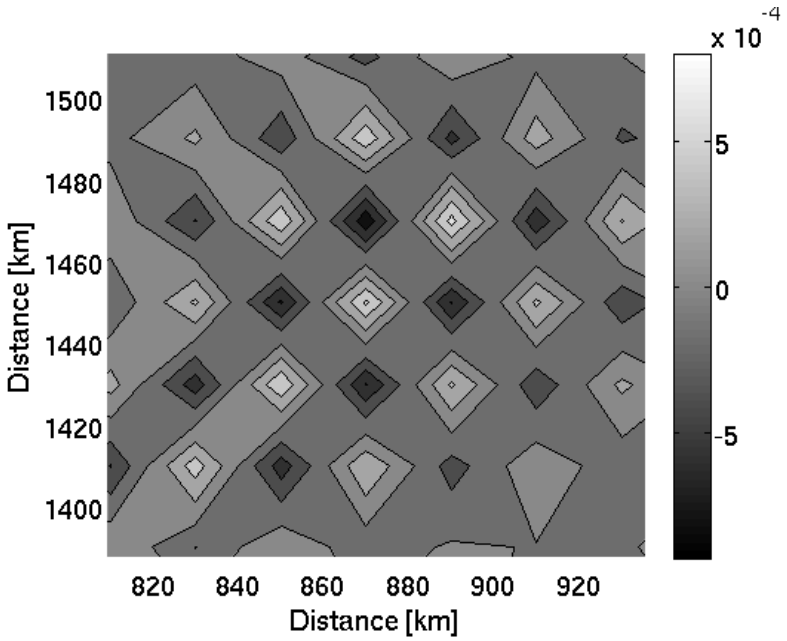

Figure 4.16: The vertical velocities [$\mathrm{m\,s^{-1}}$] at 100 m depth after 150 days in B3 with tanh stratification. The horizontal advection of the density field is included; $A_M = 400\,\mathrm{m^2\,s^{-1}}$

in the pattern can be interpreted as waves that are $2\Delta x$ long.

An explanation to why internal gravity waves were not created in Subsection 4.2.1, might have been that the density was not allowed to travel in the horizontal direction. Here it has been observed that including the horizontal advection does help to create waves. However, it is not observed waves that are affected by the Coriolis force. It is reasonable to believe that internal waves, that travel around the basin, would be generated if the Coriolis parameter f was reduced.

4.3 Diffusive fluxes

The problem of "horizontal" density diffusion in a σ-coordinate system is related to the pressure gradient errors [Beckmann and Haidvogel, 1993]. The approximation of the density diffusion often gives large truncation errors given the new coordinate system [Stelling and Van Kester, 1994]. The change in the vertical density, along sigma surfaces, tends to smooth out as a result of the diffusion. This may create artificial geostrophic flow. Mellor et al. [1998] found that new kinds of errors were added when the horizontal diffusion was included. In the previous tests the density diffusion was set to zero, see Section 1.2.

By adding diffusivity to the artificial formations, found in the plot of the vertical velocities (Figure 4.5), they might be reduced. Accordingly, the maximum velocities should become lower. Since the diffusive fluxes both increase and decrease the errors, it might be interesting to observe how the model is affected by the different approaches. Here the horizontal diffusion A_H is set equal to the horizontal viscosity $A_M = 400\,\mathrm{m^2\,s^{-1}}$.

When the diffusion is included, the maximum velocities do not have a sudden growth after 90 days, as in Figure 3.6. The velocity increases steadily throughout the 180 days, see Figure 4.17. Also note that the maximum velocities have increased. After 10 days not much difference in the vertical velocity field is seen, compare Figures 4.5 and 4.18, and Figures 4.6 and 4.19. The magnitudes of vertical velocities are reduced a little, but are approximately the same. This can also be seen in Figure 4.20. The period T is still observed to be approximately $\frac{2\pi}{f}\,\mathrm{s}$, see Figure 4.20. In Figure 4.21 the vertical velocities after 150 days are shown. By comparing to the initial acceleration of the vertical integrated divergence (Figure 4.10) it is noticed that the four distinctive formations are located at the same positions in both plots. It seems as if the Coriolis force has had a small effect on the solution, since the formations are asymmetrical.

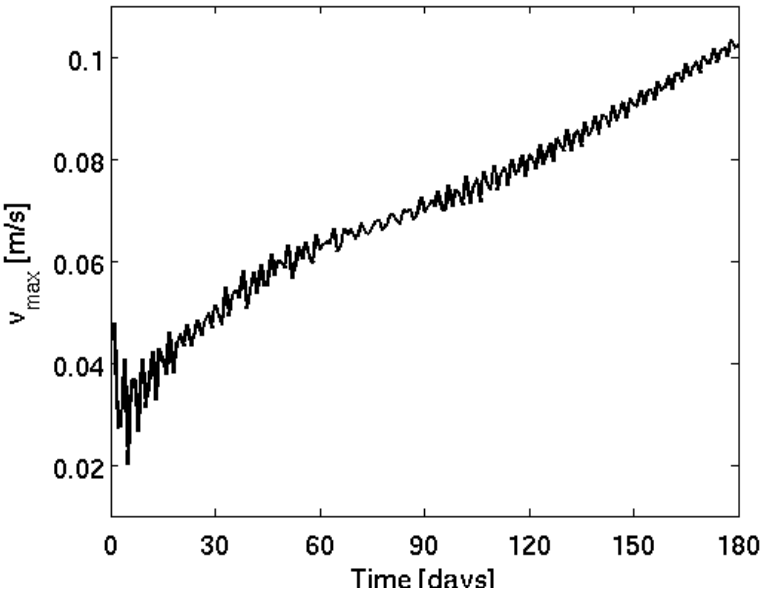

Figure 4.17: The maximum velocities $[\mathrm{m\,s^{-1}}]$ as a function of time in days for B3 with tanh stratification. The diffusive fluxes are added; $A_M = 400\,\mathrm{m^2\,s^{-1}}$

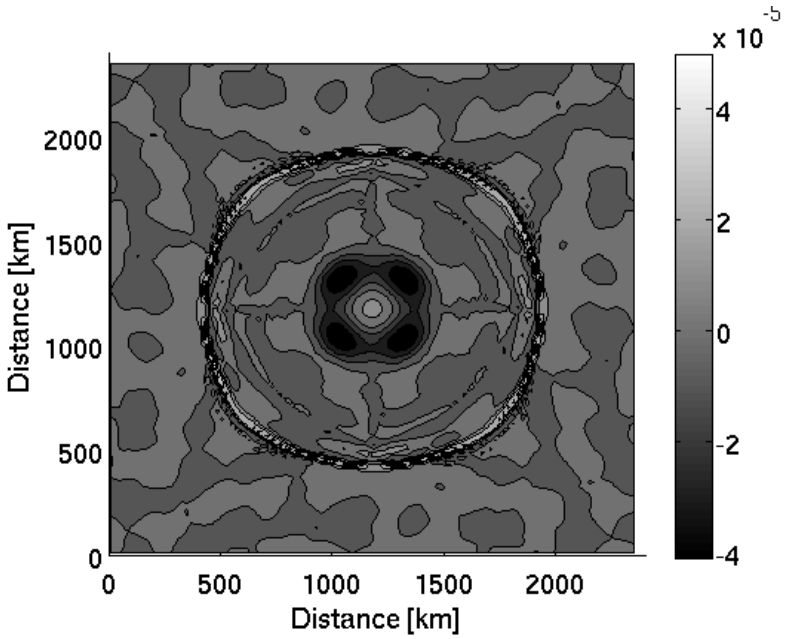

Figure 4.18: The vertical velocities [$\mathrm{m\,s^{-1}}$] at 100 m depth after 10 hours in B3 with tanh stratification. The diffusive fluxes are added; $A_M = 400\,\mathrm{m^2\,s^{-1}}$

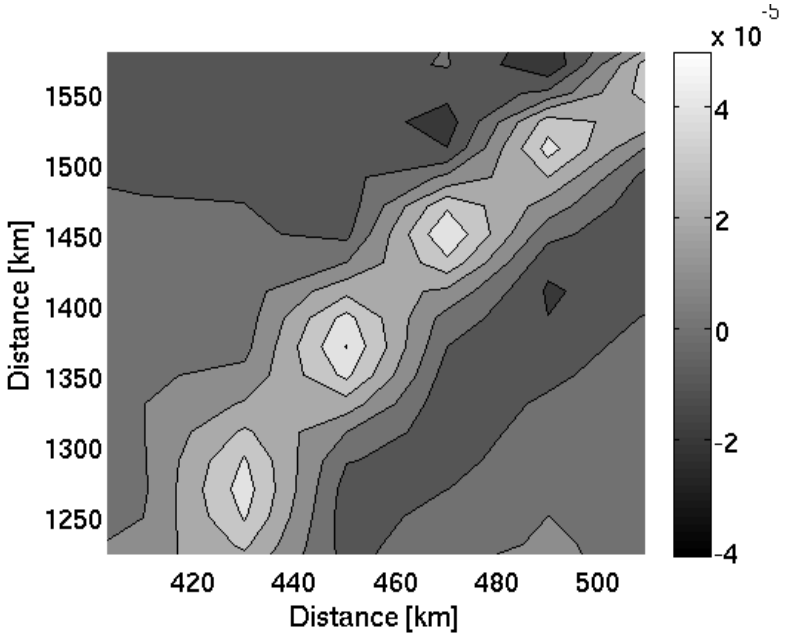

Figure 4.19: The vertical velocities [$\mathrm{m\,s^{-1}}$] at 100 m depth after 10 hours in B3 with tanh stratification. The diffusive fluxes are added; $A_M = 400\,\mathrm{m^2\,s^{-1}}$

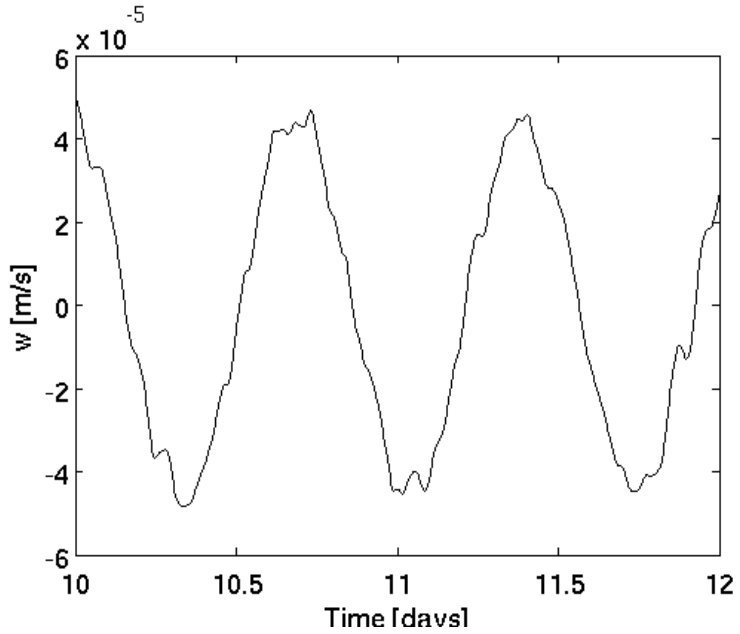

Figure 4.20: The vertical velocities [$\mathrm{m\,s^{-1}}$] as a function of time in days for B3 with tanh stratification, in the cell situated at (450 km,1370 km) at 100 m depth. The diffusive fluxes are added; $A_M = 400\,\mathrm{m^2\,s^{-1}}$

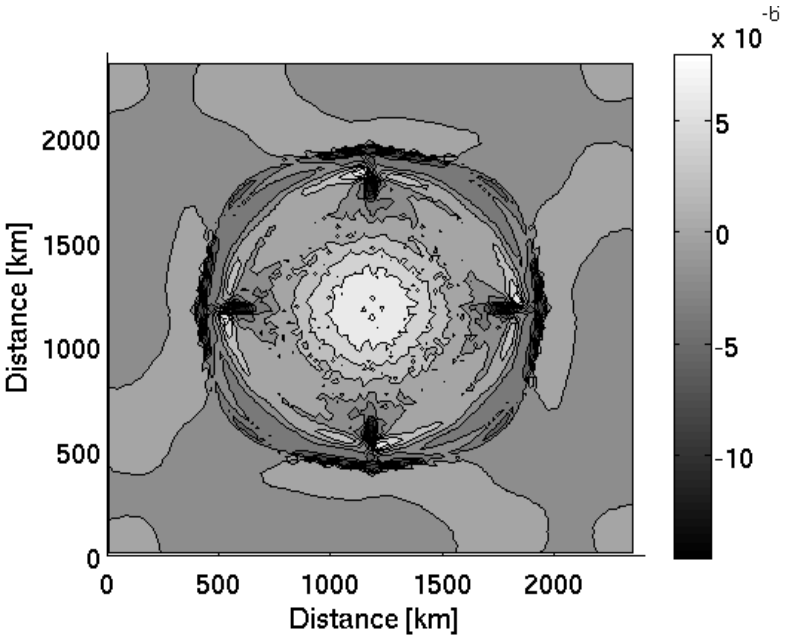

Figure 4.21: The vertical velocities [$\mathrm{m\,s^{-1}}$] at 100 m depth after 150 days in B3 with tanh stratification. The diffusive fluxes are added; $A_M = 400\,\mathrm{m^2\,s^{-1}}$

It is difficult to anticipate how the added diffusivity will affect the solution after a longer run. By the results it might seem as the new plots have more noise. Therefore one may assume that errors added by the diffusive fluxes make the solution unstable at an earlier stage.

Mellor et al. [1998] concluded that the smallest errors were observed when the ratio $\frac{A_H}{A_M} = 0$. The largest errors were observed when the ratio was 1.0. These results agree with the observations above. Following Mellor and Blumberg [1985] errors are created since A_H has a constant value. When there is no motion and density is a function of z, the horizontal diffusivity, normal to a sloping bottom, should be zero. As a consequence, there will be generated a false flow. The above problem is not only found in σ-coordinates models, but probably in all ocean models [Mellor et al., 1998].

4.4 Discussion on sigma errors

It was observed that the new test case, B3, has vorticity errors. The errors are stationed close to the steep topography. Analogous to the seamount case, the number of vortices change in time. They also travel in the beginning before they become stationary. New bathymetry has shown that the errors are affected by the topography. The open surroundings around the seamount may be the reason to why the vortices are more spread out than in B3. Another reason may be that the vortices follow isolines of the topography as a result of conservation of potential vorticity.

The plot of the vertical velocities revealed a pattern (Figure 4.5). By investigating the vertical velocity in given points in the pattern one found that the velocity oscillated with a constant period. Two experiments were implemented to shed light on the behaviour. The first investigated the initial acceleration of the horizontal divergence. It showed that there also are errors connected to the divergence. From now on these errors will be referred to as sigma errors of the third kind (SETK). Secondly, the inclusion of the horizontal advection of the density field showed that the $2\Delta x$ noise observed in the plot of the vertical velocities (Figure 4.6) can be reduced (Figure 4.13). On the other hand, it was observed that the maximum velocities grew, and that a new $2\Delta x$ noise developed. It is assumed that the results reflect the nonlinearity of the model.

The horizontal diffusivity was added to observe how the solution was affected. From the results above one can conclude that the errors were increased. The diffusion may have reduced the oscillations a fraction and made the growth of the maximum velocities more smooth, but the added errors do seem to make the model more unstable.

Chapter 5

Sensitivity to the advection scheme

The leap-frog scheme used in POM, is known to be too dispersive, while an other scheme, upwind, is too dissipative [Yang and Przekwas, 1992]. The given central difference scheme is used to solve the advective term in the conservation equation for density. By changing the scheme in the approximation of the vertical advective flux divergence term $w\frac{\partial \rho_{ref}}{\partial z}$ (Equation (1.6)), the numerical stability should be affected.

5.1 Upwind scheme

In the following figures the maximum and the vertical velocities are found, when the upwind scheme is used for the vertical advection of the reference density. Near the steep gradients the new scheme may eliminate some of the spurious $2\Delta x$ noise observed earlier (Figure 4.6). In contrast to the leap-frog scheme it has a strong numerical dissipation [Yang and Przekwas, 1992]. Note that the density can not exceed or go below the maximum and minimum values of the initial density, as long as the CFL criterion is met [Haidvogel and Beckmann, 1999].

As expected, the results show that the new scheme is more unstable. The growth of the errors is related to the advection of the density field. A new pattern is created, it reflects that the new scheme does not use central differences, see Figures 5.1, 5.2, 5.3.

Notice that the same pattern was observed in Subsection 4.2.3 when the horizontal advection of the density field was studied (Figure 4.16). Even if the formations are the same one may assume that they are created for two different reasons, the fact that nonlinear equations were used and that the upwind scheme is not centred in time and space.

Note the four distinct formations that appear equally spread on the circle. They can be observed at all times.

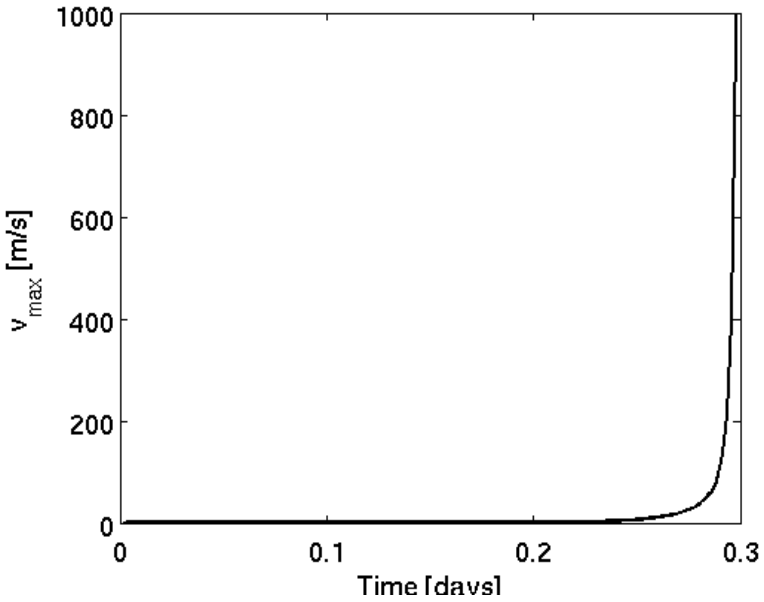

Figure 5.1: The maximum velocities [$\mathrm{m\,s^{-1}}$] at 100 m depth as a function of time in days for B3 with tanh stratification. The upwind scheme is used; $A_M = 400\,\mathrm{m^2\,s^{-1}}$

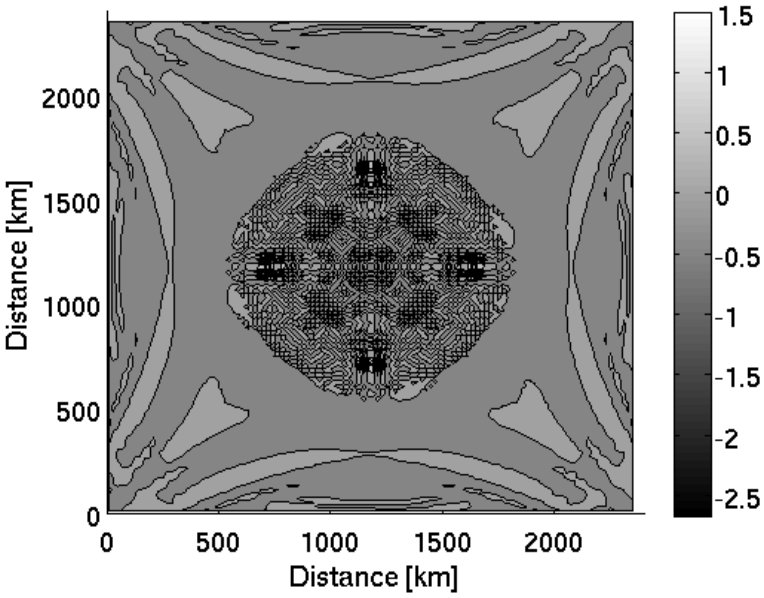

Figure 5.2: The vertical velocities [$\mathrm{m\,s^{-1}}$] at 100 m depth after 7 hours in B3 with tanh stratification. The upwind scheme is used; $A_M = 400\,\mathrm{m^2\,s^{-1}}$

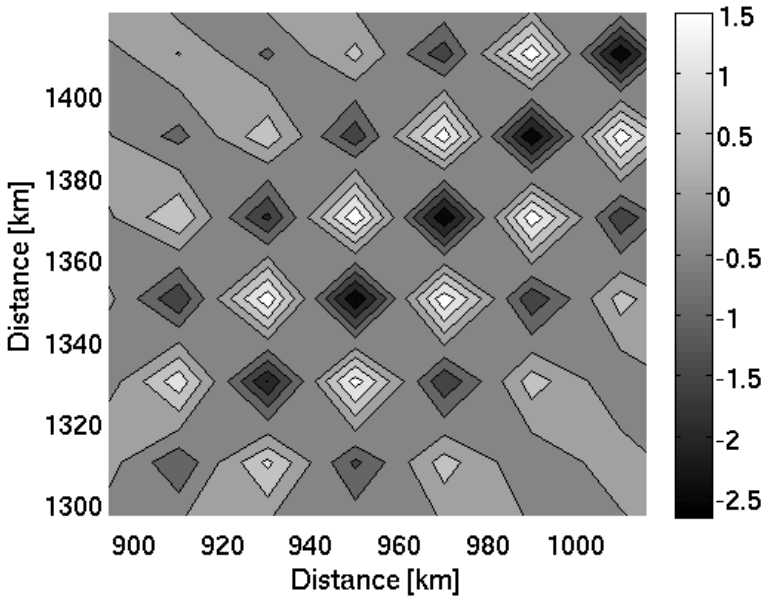

Figure 5.3: The vertical velocities [$\mathrm{m\,s^{-1}}$] at 100 m depth after 7 hours in in one part of B3 with tanh stratification. The upwind scheme is used; $A_M = 400\,\mathrm{m^2\,s^{-1}}$

5.2 TVD scheme

The Total Variation Diminishing (TVD) scheme tries to combine the good properties of the upwind scheme and a higher order scheme. The higher order scheme is used as much as possible [Yang and Przekwas, 1992], while the upwind scheme is included near steep topography. By adding dissipation, with the upwind scheme, the artificial oscillations may be reduced. Here the TVD scheme, used in the Bergen Ocean Model (BOM), is tested [Berntsen, 2000].

The TVD scheme does not improve the stability of the solution, see Figure 5.4. The growth of the maximum velocities is similar to the increase found when studying the upwind scheme, see Figure 5.1. Notice that the pattern of the vertical velocities (Figures 5.5 and 5.6) displays a $2\Delta x$ noise at the steep slope. This is the same type of formations as shown in the above test with the upwind scheme (Figure 5.2). The characteristic formations observed in the north, east, south and west of the circular slopes in the prior tests, can here be observed as an unclear cross in the circle. With the above discussion in mind, one may assume that the poor results are a consequence of the weighting of the scheme.

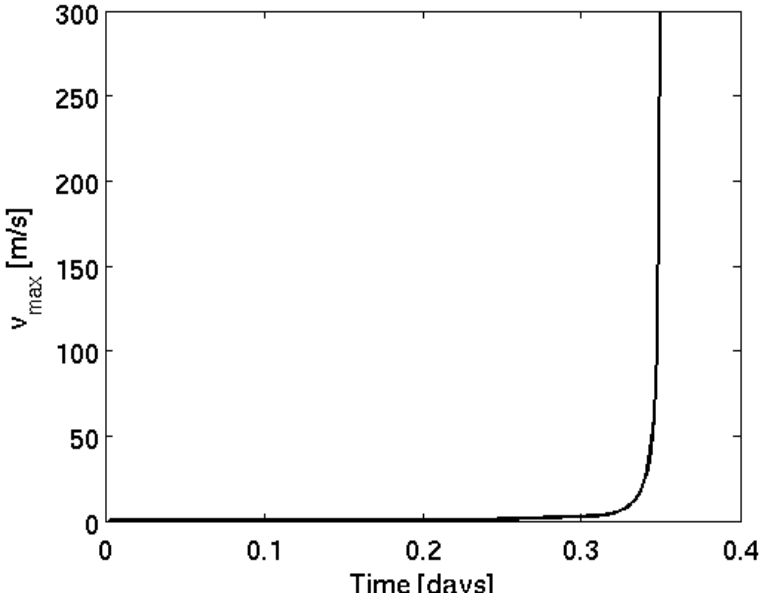

Figure 5.4: The maximum velocities [$\mathrm{m\,s^{-1}}$] at 100 m depth as a function of time in days for B3 with tanh stratification. The TVD scheme is used; $A_M = 400\,\mathrm{m^2\,s^{-1}}$

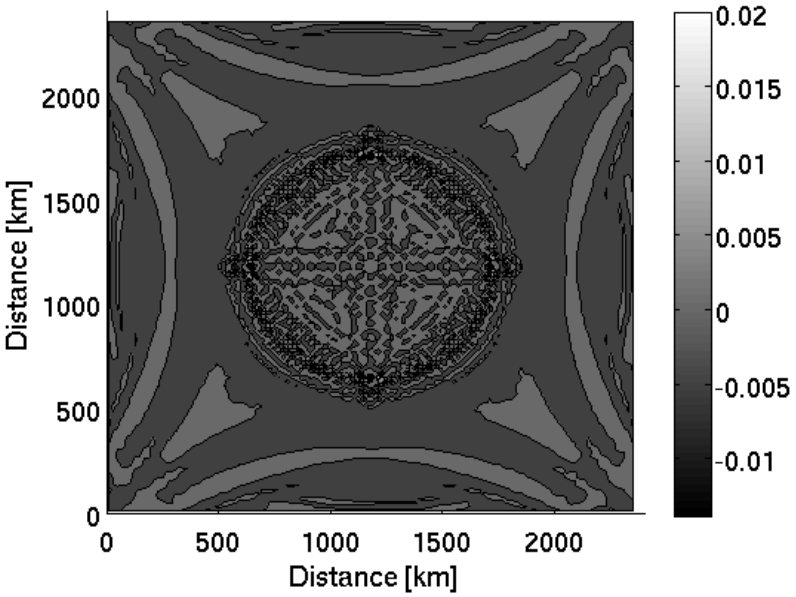

Figure 5.5: The vertical velocities [$\mathrm{m\,s^{-1}}$] at 100 m depth after 7 hours in B3 with tanh stratification. The TVD scheme is used; $A_M = 400\,\mathrm{m^2\,s^{-1}}$

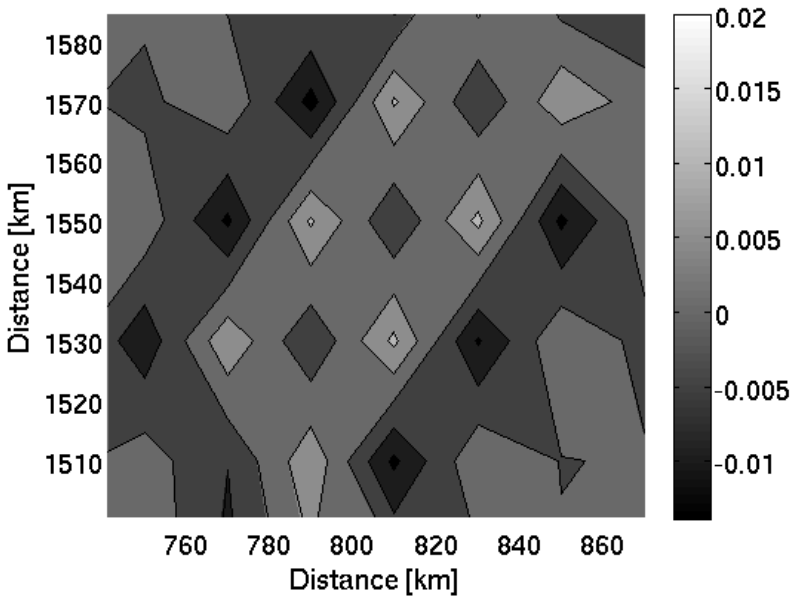

Figure 5.6: The vertical velocities [$\mathrm{m\,s^{-1}}$] at 100 m depth after 7 hours in B3 with tanh stratification. The TVD is used; $A_M = 400\,\mathrm{m^2\,s^{-1}}$

5.3 Discussion on advection schemes

The tests show that the scheme chosen for the advective term in the conservation equation for density is of great importance. While the upwind scheme was assumed to make the results worse, the TVD scheme should have made the results better. Instead, the TVD scheme tested performed almost as bad as the upwind scheme. A different TVD scheme [Yang and Przekwas, 1992] or a different weighting may have given different results.

Chapter 6

Discussion

There are several ways of forming a coordinate system. When it comes to ocean modelling, three different systems are widely used. The first is the traditional Cartesian system, the two others are terrain following (σ) and isopycnal (ρ) coordinate systems. A transformation in the vertical coordinate may be advantageous in some applications. All three classes of models have both good and bad aspects. In POM, σ-coordinates are used. A fine resolution at the surface and at the bottom is therefore achieved. In addition, all vertical layers are mapped into the ocean. One of the main concerns is the truncation errors, connected to the estimation of the internal pressure gradient. These errors often become large near steep bathymetry. If there is no external forcing and the initial density profile only depends on the vertical coordinate, no flow should be detected. The artificial velocities may be taken as a measure of the errors. Other errors are connected to the the diapycnal diffusion. That is, the density diffusion acts along isosurfaces of σ instead of density.

Several studies of the internal pressure gradient errors have been made. The investigations have improved the understanding of the errors and improved the models. The seamount test case has been the pioneer in this work. Here new test cases of ocean basins have been developed to observe the internal pressure gradient errors. Findings in this thesis have hopefully resulted in a better understanding of the errors. It is also necessary to find methods to reduce or remove the internal pressure gradient errors in σ-coordinate ocean models.

What is found

The thesis starts with a test of two different basins. The main difference between the basins is a singularity, where the shelf meets the slope, compared

to a smooth slope. The results show that the artificial flow is greatly affected by the change in the bottom topography. It was observed that the generated velocities were situated in areas with steep bathymetry. As a consequence of the lower maximum velocities, the basin with the smooth slope was chosen for the later experiments.

Further on, the model's ability to display physical phenomena was tested. The external Kelvin waves were easily reproduced, while the internal Kelvin waves turned out to be harder to generate. The shelf in the test case was too shallow. Waves were found when the buoyancy frequency was increased and the Coriolis parameter was reduced. The model's ability to show internal waves is important, since they are ubiquitous in the ocean. Internal waves should be generated, to restore balance in the model, when the internal pressure gradient errors perturb the density field. The waves can accordingly be a measure of the errors.

Mellor et al. [1998] categorised two types of errors connected to the internal pressure gradient, sigma errors of the first kind (SEFK) and sigma errors of the second kind (SESK). SEFK are associated with 2D flow and decays prognostically to zero. The SESK are only found in 3D flows and do not die out.

In this thesis, one has experienced that the new test case generates SESK. The curvature of the formations may be the cause of the different appearances of the vortices. The lonely peak allows for wide spread vortices, while the circular basin keeps them closer to the steep topography. It is also worth to note that the vortices in the basin appear to be affected be the Coriolis force. The SESK may be reduced by replacing the second order POM method with more recent methods [Chu and Fan, 1997; Thiem and Berntsen, 2006]. Several methods have been developed for the seamount test case, it may be of interest to observe if the errors created in the basins are reduced accordingly. With a finer grid resolution, the solution may be stable with a lower viscosity. It is hard to say if the maximum velocities then are reduced or if the new viscosity makes the errors grow.

A new kind of errors has also been located and classified as sigma errors of the third kind (SETK). The new errors are connected to the horizontal divergence. Artificial convergence and divergence cause the water close to the slope to oscillate vertically. This is observed in the figures as $2\Delta x$ noise. The initial divergence is, analogous to SESK, computed with estimations involving the internal pressure gradient, see Section 4.2.2 and [Mellor et al., 1998]. With the SESK in mind, it may be possible to reduce the SETK by introducing a higher order method. By testing the methods developed for SESK, one can observe if SETK are reduced accordingly.

By adding the advection of the density field, one hoped that the errors

may be reduced. This seems not to be the case. The nonlinearity of the equations create new $2\Delta x$ noise. Circular waves were observed travelling toward the centre of the basin. One might have thought that the advection and the influence of the Coriolis could lead to internal waves that travelled counter clockwise around the oceanic basin. These waves have not been observed. By reducing the Coriolis parameter or increasing the buoyancy frequency the waves may become large enough to be reproduced in the model.

Furthermore the horizontal diffusion was added. It is know that when the density stratification only depends on the vertical coordinate and the gradients are taken along σ surfaces, there is an effective vertical diffusion. The truncation errors connected to the estimation of the fluxes increase the diffusion. In agreement with Mellor et al. [1998], adding the horizontal diffusivity made the maximum velocities grow. The smoothing of the density field in the vertical may have generated an artificial flow. The model has then been given new errors by including the horizontal diffusivity.

An alternative way of observing how the numerical approach affects the internal pressure gradient errors is investigated. The model's ability to handle the vertical advection of density is tested by changing between different numerical schemes. Of the schemes investigated the leapfrog scheme, already used as a standard in the POM code, gives the best results. Further tests with different schemes may give another result. The TVD scheme used may e.g. be tested with different weights.

In the test cases, when tanh stratification was used, the most distinct errors seem to be situated in the north, east, west and south of the circular slope. The reason may be that the basin has it's steepest slopes in the given positions. Another theory is that the locations are a result of the grid orientation. A test with a rotated grid may give more information about the phenomenon.

The way forward

As discussed in the introduction, many different approaches have been tested to deal with the internal pressure gradient errors. Here, new errors have been found and connected to the divergence. The considerable literature on the seamount case may give several ideas on how to investigate the new errors. First one may try different higher order methods and observe how they affect the SETK.

According to Marsaleix et al. [2009], the initial vorticity can be a measure of the later errors. The initial divergence may also be such a measure. Then the two errors together, may give a better understanding of the internal pressure gradient errors.

Another way of investigating the errors may be found by reducing the grid size. Internal waves may then be observed in the simulations. Travelling around the basin, these waves can be thought of as propagating errors. In long-time integrations the artificial waves may grow. A measure for the errors can then be found by observing the internal waves.

In this thesis, different basins with steep shelves have been used to investigate the internal pressure gradient errors. The new approach has revealed new aspects of the errors. Hopefully, the new observations will, in time, lead to an improved model. For the time being, the results may shed new light on the internal pressure gradient errors.

Bibliography

Barnier, B., Marchesiello, P., de Miranda, A., Molines, J.-M., and Coulibaly, M. (1998). A sigma-coordinate primitive equation model for studying the circulation in the South Atlantic. Part I: Model configuration with error estimates. *Deep-Sea Research I*, 45:543–572.

Beckmann, A. and Haidvogel, D. (1993). Numerical simulation of flow around a tall isolated seamount. Part I: Problem formulation and model accuracy. *Journal of Physical Oceanography*, 23:1736–1753.

Bergh, J. (2010). *Nonhydrostatic pressure in ocean models with focus on wind driven internal*. PhD thesis, Department of Mathematics, University of Bergen, Norway.

Berntsen, J. (2000). USERS GUIDE for a modesplit σ-coordinate numerical ocean model. Technical Report 135, Dept. of Applied Mathematics, University of Bergen, Johs. Bruns gt.12, N-5008 Bergen, Norway. 48p.

Berntsen, J. (2002). Internal pressure errors in sigma-coordinate ocean models. *Journal of Atmospheric and Oceanic Technology*, 19(9):1403–1414.

Berntsen, J., Xing, J., and Davies, A. (2007). On the sensitivity of internal waves and mixing to horizontal resolution and sub-grid scale mixing . Submitted to Ocean Modelling.

Blumberg, A. and Mellor, G. (1987). A description of a three-dimensional coastal ocean circulation model. In Heaps, N., editor, *Three-Dimensional Coastal Ocean Models*, volume 4 of *Coastal and Estuarine Series*, pages 1–16. American Geophysical Union.

Chu, P. and Fan, C. (1997). Sixth-order difference scheme for sigma coordinate ocean models. *Journal of Physical Oceanography*, 27:2064–2071.

Condie, S. (1999). Comparing the performance of z-coordinate and sigma-coordinate circulation models against observations from a diurnally strat-

ified lake. Technical Report Technical Report OEEZ-99/09, Australian Commonwealth Scientific and Industrial Research Organisation.

Cushman-Roisin, B. (1994). *Introduction to Geophysical Fluid Dynamics*. Prentice Hall. ISBN-0-13-353301-8.

Gary, J. (1973). Estimation of truncation errors in transformed coordinate, primitive equation atmospheric models. *Journal of Atmospheric Science*, 30:223–233.

Gill, A. (1982). *Atmosphere-Ocean Dynamics*. Academic Press.

Gjevik, B. (2002). Unstable and neutrally stable modes in barotropic and baroclinic shelf slope currents. Technical Report 1, Preprint Series, Mechanics and Applied Mathematics, Department of Mathematics, University of Oslo, Norway.

Haidvogel, D. and Beckmann, A. (1999). *Numerical ocean circulation modeling*, volume 2 of *Series on Environmental Science and Management*. Imperial College Press.

Haney, R. (1991). On the pressure gradient force over steep topography in sigma coordinate ocean models. *Journal of Physical Oceanography*, 21:610–619.

Kundu, P. and Cohen, I. (2004). *Fluid Mechanics*. Elsevier Academic Press.

Marsaleix, P., Auclair, F., and Estournel, C. (2009). Low-order pressure gradient schemes in sigma coordinate models: The seamount test revisited. *Ocean Modelling*, 30:169–177.

McCalpin, J. (1994). A comparison of second-order and fourth-order pressure gradient algorithms in a σ-coordinate ocean model. *International Journal for Numerical Methods in Fluids*, 18:361–383.

Mellor, G. (2003). Users guide for a three-dimensional, primitive equation, numerical ocean model. Technical report, Princeton University.

Mellor, G. and Blumberg, A. (1985). Modelling vertical and horizontal diffusivities in the sigma coordinate system. *Monthly Weather Review*, 113:1379–1383.

Mellor, G., Ezer, T., and Oey, L.-Y. (1994). The pressure gradient conundrum of sigma coordinate ocean models. *Journal of Atmospheric and Oceanic Technology*, 11:1126–1134.

Mellor, G., Oey, L.-Y., and Ezer, T. (1998). Sigma coordinate pressure gradient errors and the seamount problem. *Journal of Atmospheric and Oceanic Technology*, 15:1122–1131.

Munk, W. and Wunsch, C. (1998). Abyssal recipes II: energetics of tidal and wind mixing. *Deep-Sea Research I*, 45:1978–2010.

Pond, S. and Pickard, G. (1983). *Introductory Dynamic Oceanography*. Pergamon Press.

Shapiro, R. (1975). Linear filtering. *Math.Comp.*, 29:1094–1097.

Shchepetkin, A. and McWilliams, J. (2003). A method for computing horizontal pressure-gradient force in an oceanic model with a nonaligned vertical coordinate. *Journal of Geophysical Research*, 108(C3, 3090):doi:10.1029/2001C001047.

Slørdal, L. (1997). The Pressure Gradient Force in Sigma-Co-ordinate Ocean Models. *International Journal for Numerical Methods in Fluids*, 24:987–1017.

Song, Y. (1998). A general pressure gradient formulation for ocean models. Part I: Scheme design and diagnostic analysis. *Monthly Weather Review*, 126:3213–3230.

Stelling, G. and Van Kester, J. (1994). On the approximation of horizontal gradients in sigma coordinates for bathymetry with steep bottom slopes. *International Journal for Numerical Methods in Fluids*, 18:915–935.

Thiem, Ø. and Berntsen, J. (2006). Internal pressure errors in sigma-coordinate ocean models due to anisotropy. *Ocean Modelling*, 12:140–156.

Yang, H. and Przekwas, A. (1992). A comparative study of advanced shock-capturing schemes applied to Burgers equation. *Journal of Computational Physics*, 102:139–159.